

## Binding energies of interstellar molecules on crystalline and amorphous models of water ice by ab-initio calculations

STEFANO FERRERO,<sup>1,2</sup> LORENZO ZAMIRRI,<sup>2,3</sup> CECILIA CECCARELLI,<sup>4</sup> AREZU WITZEL,<sup>4</sup> ALBERT RIMOLA,<sup>1</sup> AND PIERO UGLIENGO<sup>2</sup>

<sup>1</sup>*Departament de Química, Universitat Autònoma de Barcelona, 08193 Bellaterra, Catalonia, Spain*

<sup>2</sup>*Dipartimento di Chimica, Università degli Studi di Torino, via P. Giuria 7, 10125, Torino, Italy*

<sup>3</sup>*Nanostructured Interfaces and Surfaces (NIS) Centre, Università degli Studi di Torino, via P. Giuria 7, 10125, Torino, Italy*

<sup>4</sup>*Univ. Grenoble Alpes, CNRS, IPAG, 38000 Grenoble, France*

(Received September 22, 2020; Revised; Accepted)

Submitted to ApJ

### ABSTRACT

In the denser and colder ( $\leq 20$  K) regions of the interstellar medium (ISM), near-infrared observations have revealed the presence of sub-micron sized dust grains covered by several layers of H<sub>2</sub>O-dominated ices and “dirtied” by the presence of other volatile species. Whether a molecule is in the gas or solid-phase depends on its binding energy (*BE*) on ice surfaces. Thus, *BEs* are crucial parameters for the astrochemical models that aim to reproduce the observed evolution of the ISM chemistry. In general, *BEs* can be inferred either from experimental techniques or by theoretical computations. In this work, we present a reliable computational methodology to evaluate the *BEs* of a large set (21) of astrochemical relevant species. We considered different periodic surface models of both crystalline and amorphous nature to mimic the interstellar water ice mantles. Both models ensure that hydrogen bond cooperativity is fully taken into account at variance with the small ice cluster models. Density functional theory adopting both B3LYP-D3 and M06-2X functionals was used to predict the species/ice structure and their *BEs*. As expected from the complexity of the ice surfaces, we found that each molecule can experience multiple *BE* values, which depend on its structure and position at the ice surface. A comparison of our computed data with literature data shows agreement in some cases and (large) differences in others. We discuss some astrophysical implications that show the importance of calculating *BEs* using more realistic interstellar ice surfaces to have reliable values for inclusion in the astrochemical models.

*Keywords:* icy dust grains – complex organic molecules – dense molecular clouds – interstellar medium – ab initio – DFT – surface modeling

### 1. INTRODUCTION

The presence of molecules in the extreme physical conditions of the interstellar medium (ISM) was considered impossible by astronomers, until the first diatomic species (CN, CH and CH<sup>+</sup>) were detected in the ISM from optical and ultraviolet transitions (Swings & Rosenfeld 1937; McKellar 1940; Douglas & Herzberg 1942). Nowadays more than 200 gaseous molecular species (including radicals and ions) have been identified in the diffuse and dense regions of the ISM, thanks to their rotational and vibrational lines in the radio to Far-Infrared (FIR) wavelengths (e.g. see the review by McGuire 2018). In the coldest ( $\leq 20$ –90 K) and densest

( $\geq 10^3$  cm<sup>-3</sup>) ISM, some of these molecules are also detected in the solid state via Near-Infrared (NIR) observations (e.g. see the review by Boogert et al. 2015).

We now know that the solid-state molecules are frozen species that envelop the sub-micron dust grains that permeate the ISM and whose refractory core is made of silicates and carbonaceous materials (e.g. Jones 2013; Jones et al. 2017). The grain iced mantles composition is governed by the adsorption of species from the gas phase and by chemical reactions occurring on the grain surfaces. For example, the most abundant component of the grain mantles is H<sub>2</sub>O, which is formed by the hydrogenation of O, O<sub>2</sub> and O<sub>3</sub> on the grain surfaces (e.g. Hiraoka et al. 1998; Dulieu et al. 2010; Oba et al. 2012).

The water-rich ice is recognized from two specific NIR bands at about 3 and 6  $\mu$ m which are associated with its O-H stretching and H-O-H bending modes, respectively (e.g.

see the review by [Boogert et al. 2015](#)). In addition, species like CO, CO<sub>2</sub>, NH<sub>3</sub>, CH<sub>4</sub>, CH<sub>3</sub>OH and H<sub>2</sub>CO have also been identified as minor constituents of the ice mantles, which, for this reason, are sometimes referred to as “dirty ices” ([Boogert et al. 2015](#)). Furthermore, the comparison between the astronomical spectroscopic observations and the laboratory spectra of interstellar ice sample analogous, principally based on the O-H stretching feature, has shown that the mantle ices very likely possess an amorphous-like structure resembling that of amorphous solid water (ASW) (e.g. [Oba et al. 2009](#); [Watanabe & Kouchi 2008](#); [Boogert et al. 2015](#)).

Ice surfaces are known to have an important role in the interstellar chemistry because they can serve as catalysts for chemical reactions which cannot proceed in the gas phase, such as the formation of H<sub>2</sub>, the most abundant molecule in ISM ([Hollenbach & Salpeter 1971](#)). Ice surfaces can catalyze reactions either by behaving as: i) passive third body, this way absorbing part of the excess of energy released in the surface processes (adsorption and/or chemical reaction) (e.g. [Pantaleone et al. 2020](#)); ii) chemical catalyst, this way directly participating in the reaction reducing the activation energies (e.g. ([Rimola et al. 2018](#); [Enrique-Romero et al. 2019, 2020](#))); and iii) reactant concentrator, this way retaining the reactants and keeping them in close proximity for subsequent reaction (e.g., CO adsorption and retention for subsequent hydrogenation to form H<sub>2</sub>CO and CH<sub>3</sub>OH (e.g. [Watanabe & Kouchi 2002](#); [Rimola et al. 2014](#); [Zamirri et al. 2019b](#))). All three processes depend on the binding energies (*BEs*) of the molecules either directly (e.g. the adsorption of the species) or indirectly (e.g. because the diffusion of a particle on the grain surfaces is a fraction of its *BE*) (see [Cuppen et al. 2017](#)). In addition, molecules formed on the grain surfaces can be later transferred to the gas phase by various desorption processes, most of which depend, again, by the *BE* of the species. In practice, *BEs* are crucial properties of the interstellar molecules and play a huge role in the resulting ISM chemical composition. This key role of *BEs* is very obvious in the astrochemical models that aim at reproducing the chemical evolution of interstellar objects, as clearly shown by two recent works by [Wakelam et al. \(2017\)](#) and [Penteado et al. \(2017\)](#), respectively.

Experimentally, the *BEs* of astrochemical species are measured by temperature programmed desorption (TPD) experiments. These experiments measure the energy required to desorb a particular species from the substrate, namely a desorption enthalpy, which is equal to the *BE* only if there are no activated processes ([He et al. 2016](#)) and if thermal effects are neglected. A typical TPD experiment consists of two phases. In the first one, the substrate, maintained at a constant temperature, is exposed to the species that have to be adsorbed coming from the gas phase. In the second phase, the temperature is increased until desorption of the ad-

sorbed species—collected and analyzed by a mass spectrometer—occurs. The *BE* is then usually extracted by applying the direct inversion method on the Polanyi-Wigner equation (e.g. [Dohnalek et al. 2001](#); [Noble et al. 2012](#)). The *BE* values obtained in this way strongly depend on the chemical composition and morphology of the substrate and also on whether the experiment is conducted in the monolayer or multilayer regime (e.g. [Noble et al. 2012](#); [He et al. 2016](#); [Chaabouni et al. 2018](#)). Another issue related to the TPD technique is that it cannot provide accurate *BBEs* for radical species as they are very reactive. In literature, there are many works that have investigated the desorption processes by means of the TPD technique (e.g. [Collings et al. 2004](#); [Noble et al. 2012](#); [Dulieu et al. 2013](#); [Fayolle et al. 2016](#); [He et al. 2016](#); [Smith et al. 2016](#)) but they have been conducted for just a handful of important astrochemical species, whereas a typical network of an astrochemical model can contain up to five hundred species and very different substrates. In a recent work, [Penteado et al. \(2017\)](#) collected the results of these experimental works, trying to be as homogeneous as possible in terms of different substrates, estimating the missing *BE* values from the available data and performing a systematic analysis on the effect that the *BE* uncertainties can have on astrochemical model simulations.

*BE* values can also be obtained by means of computational approaches which, in some situations, can overcome the experimental limitations. Many computational works have so far focused on a few important astrochemical species like H, H<sub>2</sub>, N, O, CO, CO<sub>2</sub>, in which *BEs* are calculated on periodic/cluster models of crystalline/amorphous structural states using different computational techniques (e.g. [Al-Halabi & Van Dishoeck 2007](#); [Karssemeijer et al. 2014](#); [Karssemeijer & Cuppen 2014](#); [Ásgeirsson et al. 2017](#); [Senevirathne et al. 2017](#); [Shimonishi et al. 2018](#); [Zamirri et al. 2019a](#)). In addition, other works have computed *BE* in a larger number of species but with a very approximate model of the substrate. For example, in a recent work by [Wakelam et al. \(2017\)](#) *BE* values of more than 100 species are calculated by approximating the ASW surface with a single water molecule. The authors then fitted the most reliable *BE* measurements (16 cases) against the corresponding computed ones, obtaining a good correlation between the two data sets. In this way, all the errors in the computational methods and limitations due to the adoption of a single water molecule are compensated by the fitting with the experimental values, in the view of the authors. The resulting parameters are then used to scale all the remaining computed *BE* to improve their accuracy. This clever procedure does, however, consider the proposed scaling universal, leaving aside the complexity of the real ice surface and the specific features of the various adsorbates. In a similar work, [Das et al. \(2018\)](#) have calculated the *BEs* of 100 species by increasing the size of a water cluster from one

to six molecules, noticing that the calculated  $BE$  approaches the experimental value when the cluster size is increased. As we will show in the present work, these approaches, relying on an arbitrary and very limited number of water molecules, cannot, however, mimic a surface of icy grain. Furthermore, the strength of interaction between icy water molecules as well as with respect to the adsorbates depends on the hydrogen bond cooperativity, which is underestimated in small water clusters.

In this work, we followed a different approach, focusing on extended periodic ice models, either crystalline or amorphous, adopting a robust computational methodology based on a quantum mechanical approach. We simulate the adsorption of a set of 21 interstellar molecules, whose 4 are radical species, on several specific exposed sites of the water surfaces of both extended models.  $BE$  values have been calculated for more than one binding site (if present) to provide the spread of the  $BE$  values that a same molecule can have depending on the position in the ice. Different approaches, with different computational cost, have been tested and compared, and the final computed  $BE$ s have been compared with data from the computational approaches of Wakelam et al. (2017) and Das et al. (2018) and data from UMIST and KIDA databases as well as available experimental data (e.g. McElroy et al. 2013; Wakelam et al. 2015). One added value of this work is the definition of both a reliable, computationally cost-effective ab-initio procedure designed to arrive to accurate  $BE$  values and an ice grain atomistic model, that can be applied to predict the  $BE$ s of any species of astrochemical interest.

## 2. COMPUTATIONAL DETAILS

### 2.1. Structure of the ice: periodic simulations

Water ice surfaces have been modelled enforcing periodic boundary conditions to define icy slabs of finite thickness either entirely crystalline or of amorphous nature. Adsorption is then carried out from the void region above the defined slabs. Periodic calculations have been performed with the ab initio CRYSTAL17 code (Dovesi et al. 2018). This software implements both the Hartree-Fock (HF) and Kohn-Sham self-consistent fields methods for the solution of the electronic Schrödinger equation, fully exploiting, if present, the crystalline or molecular symmetry of the system under investigation. CRYSTAL17 adopts localized Gaussian functions as basis sets, similar to the approach followed by molecular codes. This allows CRYSTAL17 to perform geometry optimizations and vibrational properties of both periodic (polymer, surfaces and crystals) and non-periodic (molecules) systems with the same level of accuracy. Furthermore, the definition of the surfaces through the slab model allows to avoid the 3D fake replica of the slab as forced when adopting plane waves basis set.

Computational parameters are set to values ensuring good accuracy in the results. The threshold parameters for the evaluation of the Coulomb and exchange bi-electronic integrals (TOLINTEG keyword in the CRYSTAL17 code; Dovesi et al. (2018)) have been set equal to 7, 7, 7, 7, 14. The needed density functional integration are carried out numerically over a grid of points, which is based on an atomic partition method developed by Becke (1988). The standard pruned grid (XLGRID keyword in the CRYSTAL17 code; Dovesi et al. (2018)), composed by 75 radial points and a maximum of 974 angular points, was used. The sampling of the reciprocal space was conducted with a Pack-Monkhorst mesh (Pack & Monkhorst 1977), with a shrinking factor (SHRINK in the code CRYSTAL17; Dovesi et al. (2018)) of 2, which generates 4  $k$  points in the first Brillouin zone. The choice of the numerical values we assigned to these three computational parameters is fully justified in the Appendix A.

Geometry optimizations have been carried out using the Broyden-Fletcher-Goldfarb-Shanno (BFGS) algorithm (Broyden 1970; Fletcher 1970; Goldfarb 1970; Shanno 1970), relaxing both the atomic positions and the cell parameters. We adopted the default values for the parameters controlling the convergence, i.e., difference in energy between two subsequent steps,  $1 \times 10^{-7}$  Hartree; and maximum components and root-mean-square of the components of the gradients and atomic displacements vectors,  $4.5 \times 10^{-4}$  Hartree Bohr<sup>-1</sup> and  $3 \times 10^{-4}$  Hartree Bohr<sup>-1</sup>, and  $1.8 \times 10^{-3}$  Bohr and  $1.2 \times 10^{-3}$  Bohr, respectively. All periodic calculations were grounded on either the density functional theory (DFT) or the HF-3c method (Hohenberg & Kohn 1964; Sure & Grimme 2013). Within the DFT framework, different functionals were used to describe closed- and open-shell systems. For the former, we used the hybrid B3LYP method (Becke 1993; Lee et al. 1988), which has been shown to provide a good level of accuracy for the interaction energies of non-covalent bound dimers (Kraus & Frank 2018), added with the D3-BJ correction for the description of dispersive interactions (Grimme et al. 2010, 2011). For open-shell systems, treated with a spin-unrestricted formalism (Pople et al. 1995), we used the hybrid M06-2X functional (Zhao & Truhlar 2008), which has been proved to give accurate results in estimating the interaction energy of non-covalent binary complexes involving a radical species and a polar molecule (Tentscher & Arey 2013). The choice of these two different functionals is justified by two previous works describing the accuracy on the energetic properties of molecular adducts (Kraus & Frank 2018; Tentscher & Arey 2013). For all periodic DFT calculations we used the Ahlrichs' triple-zeta quality VTZ basis set, supplemented with a double set of polarization functions (Schäfer et al. 1992). In the following, we will refer to this basis set as "A-VTZ\*" (see Appendix D for details of the adopted basis set).

The HF-3c method is a new method combining the Hartree-Fock Hamiltonian with the minimal basis set MINI-1 (Tatewaki & Huzinaga 1980) and with three a posteriori corrections for: i) the basis set superposition error (BSSE), arising when localized Gaussian functions are used to expand the the basis set (Jansen & Ros 1969; Liu & McLean 1973); ii) the dispersive interactions; iii) short-ranged deficiencies due to the adopted minimal basis set (Sure & Grimme 2013).

Harmonic frequency calculations were carried out on the optimized geometries of both crystalline and amorphous ices to characterize the stationary points of each structure. Vibrational frequencies have been calculated at the  $\Gamma$  point by diagonalizing the mass-weighted Hessian matrix of second order energy derivatives with respect to atomic displacements (Pascale et al. 2004; Zicovich-Wilson et al. 2004). The Hessian matrix elements have been evaluated numerically by a six-points formula (NUMDERIV=2 in the CRYSTAL17 code; Dovesi et al. (2018)), based on two displacements of  $\pm 0.003$  Å for each nuclear cartesian coordinates from the minimum structure.

To avoid computational burden, only a portion of the systems has been considered in the construction of the Hessian matrix, including the adsorbed species and the spatially closest interacting water molecules of the ice surface. This “fragment” strategy for the frequency calculation has already been tested by some of us in previous works and is fully justified by the non-covalent nature of the interacting systems where the coupling between the vibrational modes of bulk ice and adsorbate moieties is negligible (Tosoni et al. 2005; Rimola et al. 2008; Zamirri et al. 2017).

From the set of frequencies resulting from the “fragment” calculations we worked out the zero point energy (ZPE) for the free crystalline ice surface, the free adsorbate, the ice-surface/adsorbate complex to arrive to the corresponding correction  $\Delta ZPE$ , as reported in Appendix A.1. From the  $\Delta ZPE$  we corrected the electronic  $BE$  for each adsorbates as:  $BE(0) = BE - \Delta ZPE$  and found a good linear correlation  $BE(0)=0.854 BE$ , as shown in Figure 13 of the Appendix A.1. While the “fragment frequency” strategy is fine for computing the  $\Delta ZPE$  of the crystalline ice model due to the structural rigidity enforced by the system symmetry, the same does not hold for the amorphous ice. In that case, the large unit cell (60 water molecules) and their random organization renders the ice structure rather sensitive to the adsorbate interaction which causes large structural water molecules rearrangement. This, in turn, alter significantly the whole set of normal modes and the numerical value of the  $\Delta ZPE$  becomes ill-defined. Nevertheless, considering that the kind of interactions operative for the crystal ice are of the same nature of those for the amorphous one, we adopted the same scaling factor 0.854 computed for the crystalline ice to correct the electronic  $BE$  for the amorphous one. In the fol-

lowing, we compared the experimental  $BE$  usually measured for amorphous ices with the  $BE(0)$  values. To discuss the internal comparison between adsorption features of different adsorbates on the crystalline ice, we still focused on the uncorrected  $BE$ s.

## 2.2. Binding energies calculation and Counterpoise correction

When Gaussian basis sets are used, a spurious contribution arises in the calculation of the molecule/surface interactions, called BSSE (basis set superposition error) (e.g. Boys & Bernardi 1970). In this work, the BSSE for DFT calculations has been corrected making use of the a posteriori Counterpoise correction (CP) by Boys and Bernardi (Davidson & Feller 1986). The CP-corrected interaction  $\Delta E^{CP}$  energy has been calculated as

$$\Delta E^{CP} = \Delta E^* + \delta E + \Delta E_L - BSSE \quad (1)$$

where  $\Delta E^*$  is the deformation free interaction energy,  $\delta E$  is the total contribution to the deformation energy, and  $\Delta E_L$  is the lateral interaction (adsorbate-adsorbate interaction) energy contribution. Details on the calculation of each energetic term of Eq. (1) can be found in the Appendix A. By definition,  $BE$  is the opposite of the CP-corrected interaction energy:

$$\Delta E^{CP} = -BE \quad (2)$$

## 2.3. BE refinement with the embedded cluster method

With the aim of refining the periodic DFT  $BE$  values for the crystalline ice model, single point energy calculations have been carried out on small clusters, cut out from the crystalline ice model, using a higher level of theory than the DFT methods with the Gaussian09 program (Frisch et al. 2009). The adopted cluster models were derived from the periodic systems and are described in § 3.2.2. These refinements have been performed through the ONIOM2 approach (Dapprich et al. 1999), dividing the systems in two parts that are described by two different levels of theory. The *Model system* (i.e., a small moiety of the whole system including the adsorbate and the closest water molecules) was described by the *High* level of theory represented by the single- and double-electronic excitations coupled-cluster method added with a perturbative description of triple excitations (CCSD(T)). The *Real system* (i.e., the whole system) was described by the DFT level of theory adopted in the periodic calculations with the two different functionals for open- and closed-shell species. In the ONIOM2 methodology, the  $BE$  can be written as:

$$BE(ONIOM2) = -BE(Low, Real) + \Delta BE \quad (3)$$

$$\Delta BE = BE(High, Model) - BE(Low, Model) \quad (4)$$

The final BE(ONIOM2) is also corrected by the BSSE following the same scheme described above. Our choices about the *Model* and *Real system* will be extensively justified in § 3.2.2.

### 3. RESULTS

#### 3.1. Ice surface models

##### 3.1.1. Crystalline ice model

Despite the amorphous and perhaps porous nature of the interstellar ice, we adopted, as a paradigmatic case, a proton-ordered crystalline bulk ice model usually known as *P-ice* ( $Pna2_1$  space group) (Casassa et al. 1997). From P-ice bulk, we cut out a slab model i.e. a 2D-periodic model representing a surface. Consequently, periodic boundary conditions are maintained only along the two directions defining the slab plane, while the third direction ( $z$ -axis) is non-periodic and defines the slab thickness. The slab model adopted in this work represents the P-ice (010) surface, in accordance with previous work (Zamirri et al. 2018). This slab consists of twelve atomic layers, is stoichiometric and has a null electric dipole moment across the  $z$ -axis. This ensures an electronic stability of the model with the increase of the slab thickness (Tasker 1979). The slab structure has been fully optimized (unit cell and atomic fractional coordinates) at both B3LYP-D3/A-VTZ\* and M06-2X/A-VTZ\* DFT levels. As it can be seen from Figure 1 (panel A) the (010) P-ice unit cell is rather small, showing only one dangling hydrogen (dH) and oxygen (dO) as binding sites. For large molecules, to increase the number of adsorption sites and minimize the lateral interactions among replicas of the adsorbate we also considered a 2x1 supercell. The electrostatic potential maps (EPMs, see Fig. 1, panels B and C), clearly reveal positive (blue EPM regions) and negative (red EPM regions) potentials around the dH and dO sites, respectively.

##### 3.1.2. Amorphous solid water (ASW)

As anticipated, the (010) P-ice surface might not be a physically sound model to represent actual interstellar ice surfaces, due to the evidence, from the spectroscopic feature of the interstellar ice, of its amorphous nature (Boogert et al. 2015). The building up of amorphous surface models is a non-trivial and not unique procedure, because of the lack of a consistent and universally-accepted strategy. One common approach is to start from a crystalline model and heat it up to relatively high temperature by running molecular dynamics simulations (MDs) for few picoseconds. This step is followed by thermal annealing to freeze the ice in a glassy amorphous state. In this work, we adopted a different strategy. We refer to a recent work by Shimonishi et al. (2018) in which the *BEs* of a set of atomic species were computed on several water clusters, previously annealed with MD simulations. We re-optimized (at B3LYP-D3/A-VTZ\* level only)

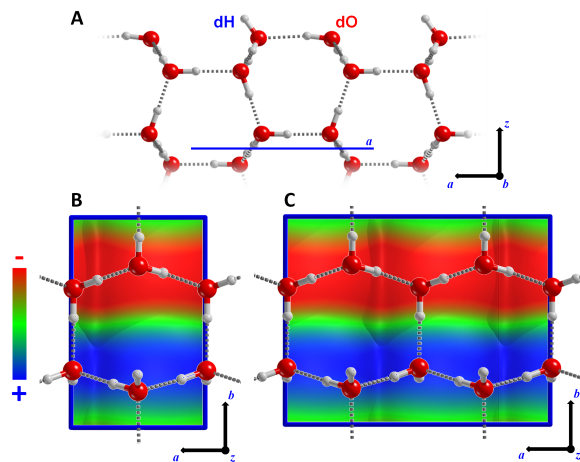


**Figure 1.** (010) slab model of P-ice. A) Side view along the  $b$  lattice vector. B) Top view of the 1x1 unit cell ( $|a| = 4.500 \text{ \AA}$  and  $|b| = 7.078 \text{ \AA}$ ) superimposed to the electrostatic potential map, EPM. C) Top view of the 2x1 supercell ( $|a| = 8.980 \text{ \AA}$ ,  $|b| = 7.081 \text{ \AA}$ ) superimposed to the EPM. The iso-surface value for the electron density where the electrostatic potential is mapped is set equal to  $10^{-6}$  au. Colour code: +0.02 au (blue, positive), 0.00 au (green, neutral) and -0.02 au (red, negative).

the whole set of ice clusters and the three most stable clusters, composed by 20 water molecules each, were merged together to define a unit cell of an amorphous periodic ice. This procedure mimics somehow the collision of nanometric scale icy grains occurring in the molecular clouds. The merge of the three clusters was carried out by matching the dHs regions of one cluster with the dOs ones of the other. As a result, we ended up with a large 3D-periodic unit cell (with lattice parameters  $|a| = 21.11 \text{ \AA}$ ,  $|b| = 11.8 \text{ \AA}$  and  $|c| = 11.6 \text{ \AA}$ ) envisaging 60 water molecules. This initial bulk model was optimized at HF-3c level in order to fully relax the structure from the internal tensions of the initial guess. After this step, we cut out a 2D-periodic slab from the bulk structure. The amorphous slab is composed by 60 water molecules in the unit cell, and was further fully optimized (unit cell size and atomic coordinates) at the HF-3c level, B3LYP-D3/A-VTZ\* and M06-2X/A-VTZ\* levels of theory. The three final structures show little differences in the positions of specific water molecules and, on the whole, the structures are very similar (Fig. 2). The computed electric dipole moment across the non-periodic direction (1.2, 0.7 and 0.1 Debyes for the HF-3c, B3LYP-D3 and M06-2X structures, respectively) showed a very good agreement between different models, also considering the dependence of the dipole value on the adopted quantum mechanical method. These amorphous slab models show different structural features for the upper and lower surfaces which imparts the residual dipole moment across the slab, and, consequently, exhibit a variety of different binding sites for adsorbates. To characterize the electrostatic features

of these sites, which in turn dictate the adsorption process, we resorted to the EPMS for the top/bottom surfaces of each optimized slab (Fig. 3). The general characteristics are very similar for the three models: B3LYP-D3 and M06-2X giving the closest maps. HF-3c tends to enhance the differences between positive/negative regions due to overpolarization of the electron density caused by the minimal basis set. “Top” surfaces show a hydrophobic cavity (the central greenish region, Fig. 3, absent in the P-ice slab, surrounded by dHs positive spots. “Bottom” surfaces shows several prominent negative regions (from five dOs) mixed with less prominent positive potentials (due to four buried dHs).

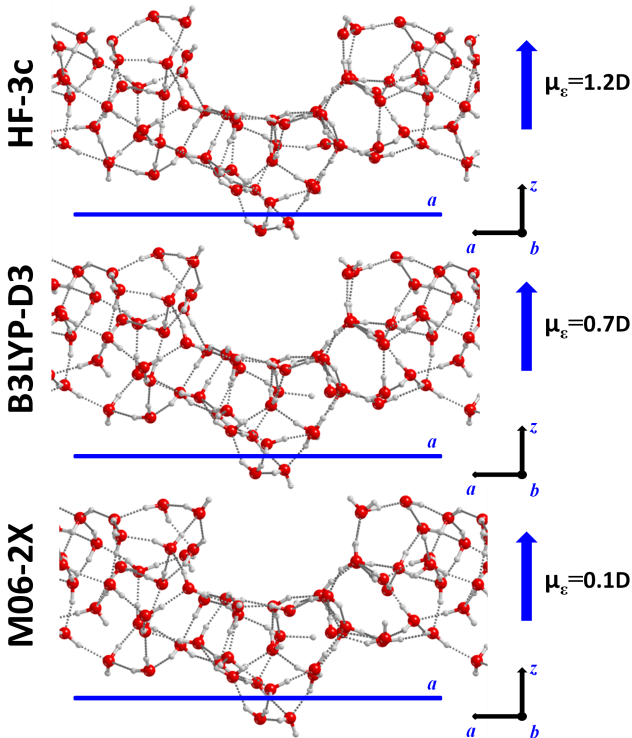


**Figure 2.** Side view of the amorphous slab models. The cell parameter  $a$  is highlighted as a blue line. Electric dipole moments  $\mu_\epsilon$  along the  $z$  direction are shown on the right side.

### 3.2. BEs on crystalline ice

#### 3.2.1. BE computed with DFT/DFT method

In this work, we simulated the adsorption of 17 closed-shell species and 4 radicals, shown in Fig. 4. For each molecule/surface complex, geometry optimizations (unit cell plus all atomic coordinates without constraints) were performed. Initial structures were guessed by manually setting the maximum number of H-bonds between the two partners. The pure role of dispersion is estimated by extracting the D3 contribution from the total energy at B3LYP-D3 level of theory. The energetics of the adsorption processes were then computed according to Eq. (1).

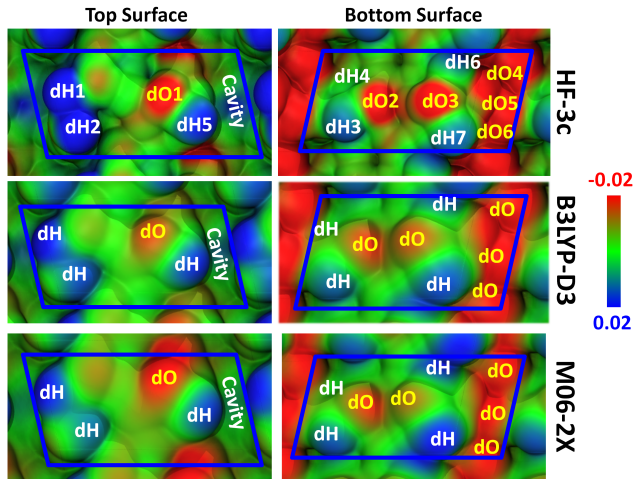


**Figure 3.** Colour-coded electrostatic potential energy maps (EPMS) mapped to the electron density for the “top” and “bottom” surfaces of the amorphous slab (HF-3c, B3LYP-D3 and M06-2X optimized geometries). dO and dH sites are also labelled. The iso-surface value for the electron density is set equal to  $10^{-6}$  au to which the electrostatic potential is mapped out. EPM color code: +0.02 au (blue, positive), 0.00 au (green, neutral) and -0.02 au (red, negative)..

As it can be seen from the results of Table 1, a range of interactions of different strength is established between the adsorbed species and the crystalline P-ice surface. Some molecules do not possess a net electric dipole moment, while exhibiting relevant electric quadrupole moments (i.e.,  $H_2$ ,  $N_2$  and  $O_2$ ) or multipoles moments of higher order (i.e.,  $CH_4$ , see their EPMS in B). For these cases, only weak interactions are established so that  $BE$ s are lower than 1800 K (see  $BE$  disp values in Table 1). Interestingly, for the  $N_2$ ,  $O_2$  and  $CH_4$  cases, interactions are almost repulsive if dispersive contributions are not accounted for in the total  $BE$  (compare  $BE$  disp with  $BE$  no disp values of Table 1). Therefore, the adsorption is dictated by dispersive forces, which counterbalance the repulsive electrostatic interactions. For the  $H_2$  case, electrostatic interactions are attractive mainly because of the synergic effect of both the surface dH and the dO on the negative and positive parts of the  $H_2$  quadrupole, respectively (see Fig. 16).

$CO$ ,  $OCS$  and  $CO_2$  also exhibit a quadrupole moment, but due to the presence of heteroatoms in the structure, they can also establish H-bonds with the dH site. Consequently,  $BE$ s are larger than the previous set of molecules (i.e.,  $> 2400$  K, see Table 1). For these three cases, pure electrostatic interactions are attractive, but the dispersion contribution is the most dominant one over the total  $BE$  values (compare  $BE$  disp with  $BE$  no disp values of Table 1).  $CO$ , in addition to a net quadrupole, also possesses a weak electric dipole, with the negative end at the carbon atom (see its EPM in B) (Zamirri et al. 2017). Thus, although the two negative poles (C

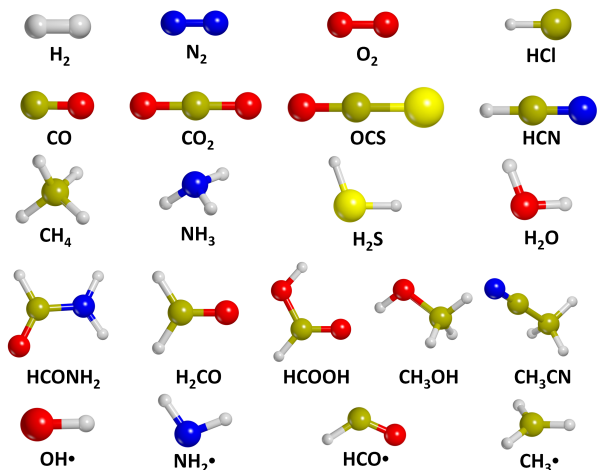


**Figure 4.** Set of molecular and radical species adopted within this work for the calculation of binding energy on different ice models.  $O_2$  is an open-shell (spin-triplet) species (Borden et al. 2017).

and O atoms) of the quadrupole, both can interact with the positive dH site, the interaction involving the C atom is energetically slightly favoured over the O atom (Zamirri et al. 2017, 2019a). Accordingly, we only considered the C-down case, the computed  $BE$  being in good agreement with previous works (Zamirri et al. 2017, 2018). OCS also possesses a dipole and can interact with the surface through either its S- or O-ends, through dO or dH sites. However, due to the softer basic character of S compared to O, the interaction through oxygen is preferred and only considered here.

$NH_3$ ,  $H_2O$ ,  $HCl$ ,  $HCN$  and  $H_2S$  are all amphiprotic molecules that can both serve as acceptors and donors of H-bonds from/to the dH and dO sites. The relative strong H-bonds with the surface result in total  $BE$  values that are almost twice higher than the values of the previous set of molecules (i.e.,  $CO$ ,  $OCS$  and  $COS$ ). Although also in these cases dispersive forces play an important contribution to the  $BE$ , the dominant role is dictated by the H-bonding contribution.

For the adsorption of  $CH_3OH$ ,  $CH_3CN$  and the three carbonyl-containing compounds, i.e.,  $H_2CO$ ,  $HCONH_2$  and  $HCOOH$ , all characterized by large molecular sizes, we adopted the 2x1 supercell (shown in Fig. 1) to minimize the lateral interactions between adsorbates. Consequently, two dHs and two dOs are available for adsorption. Therefore, for some of these species (i.e., the carbonyl-containing ones), we started from more than one initial geometry to improve a better sampling of the adsorption features on the (010) P-ice surface (the different cases on the supercell are labeled as SC1 and SC2 in Table 1 and the geometries are reported in B). The  $BE$  values of these species are among the highest ones, due to the formation of multiple H-bonds with the slab (and therefore increasing the electrostatic contribution to the inter-

actions), and a large dispersion contribution due to the larger sizes of these molecules with respect to the other species.

The adsorption study has also been extended to four radicals (i.e.,  $OH\bullet$ ,  $NH_2\bullet$ ,  $CH_3\bullet$ ,  $HCO\bullet$ ), since they are of high interest due to their role in the formation of interstellar compounds (Sorrell 2001; Bennett & Kaiser 2007).  $OH\bullet$  and  $NH_2\bullet$  form strong H-bonds with the dH and dO sites of the slab, at variance with  $CH_3\bullet$  and  $HCO\bullet$  cases, as shown by the higher  $BE$  values. Because of the nature of the M06-2X functional, we cannot separate the dispersion contributions to the total  $BEs$ . Interestingly, in all cases, we did not detect transfer of the electron spin density from the radicals to the ice surface, i.e., the unpaired electron remains localized on the radical species upon adsorption.

### 3.2.2. The ONIOM2 correction and the accuracy of the DFT//DFT $BE$ values

As described in the Computational Details section, the ONIOM2 methodology has been employed to check the accuracy of the B3LYP-D3/A-VTZ\* and M06-2X/A-VTZ\* theory levels, both representing the *Low* level of calculation. For this specific case, to reduce the computational burden, we only considered 15 species, leaving aside  $N_2$ ,  $O_2$ ,  $H_2O$ ,  $CH_4$ ,  $CH_3CN$  and  $CH_3\bullet$  radical. Here, the *Real system* is the periodic P-ice slab model without adsorbed species. Therefore, the  $BE(Low,Real)$  term in Eq. (3) corresponds to the  $BEs$  at the DFT theory levels, hereafter referred to as  $BE(DFT, Ice)$ . The *Model system* is carved from the optimized geometry of the periodic system: it is composed by the adsorbed molecule plus  $n$  ( $n = 2, 6$ ; the latter only for the  $H_2$  case) closest water molecules of the ice surface to the adsorbates. For the *Model systems*, two single point energy calculations have been carried out: one at the *High* level of theory, i.e., CCSD(T), calculated with Gaussian09, and the other at the *Low* level of theory, employing the same DFT methods as in the periodic calculations, calculated with CRYSTAL17. For the sake of clarity, we renamed the two terms  $BE(High,Model)$  and  $BE(Low,Model)$  in Eq. (3) for any molecular species  $\mu$ , as  $BE(CCSD(T), \mu-nH_2O)$  and  $BE(DFT, \mu-nH_2O)$ , respectively.

As CCSD(T) is a wavefunction-based method, the associated energy strongly depend on the quality of the adopted basis set (Cramer 2002). Consequently, accurate results are achieved only when complete basis set extrapolation is carried out (Cramer 2002); accordingly, we adopted correlation consistent basis sets (Dunning Jr 1989), here named as cc-pVNZ, where “cc” stands for correlation consistent and  $N$  stands for double (D), triple (T), quadruple (Q), etc... Therefore, we performed different calculations improving the quality of the basis set from **Jun**-cc-pVDZ to **Jun**-cc-pVQZ (and even **Jun**-cc-pV5Z when feasible) (Bartlett & Musiał 2007; Papajak et al. 2011), extrapolating the  $BE(CCSD(T), \mu-nH_2O)$  values for  $N \rightarrow \infty$ . Figure 5 shows, using  $NH_3$  as illustrative example, the plot of the  $BE(CCSD(T), \mu-nH_2O)$

values as a function of  $1/L^3$  where  $L$  is the cardinal number corresponding to the  $N$  value for each correlation-consistent basis set. For all other species, we observed similar trends. This procedure was used in the past to extrapolate the  $BE$  value of CO adsorbed at the Mg(001) surface (Ugliengo & Damin 2002).

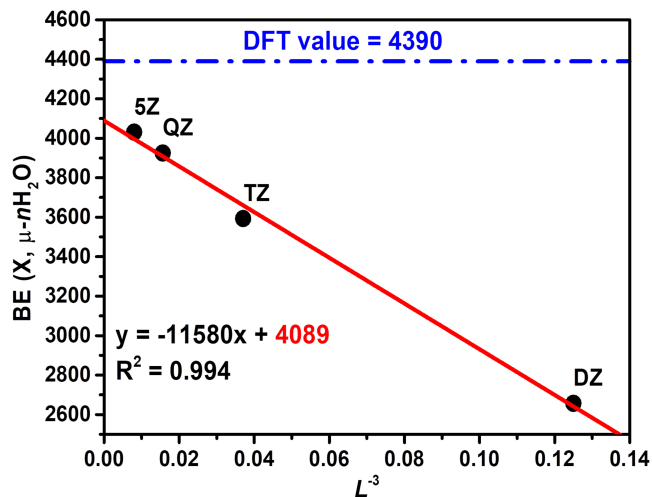


**Figure 5.**  $BE(X, \mu-nH_2O)$  extrapolated value at infinite basis set for the case of  $NH_3$ . The dashed-dot blue line represents the  $BE$  computed for the  $BE(DFT, \mu-nH_2O)$  at DFT//A-VTZ\* level (4390 K). Solid red line represents the linear fit of the  $BE(CCSD(T), \mu-nH_2O)$  values (red squares) calculated with DZ, TZ, QZ and 5Z basis sets. The extrapolated  $BE(X, \mu-nH_2O)$  at infinite basis set is highlighted in red in the fitting equation (4089 K).

The procedure gives for the extrapolated  $BE(CCSD(T), \mu-nH_2O)$  a value of 4089 K in excellent agreement with the value computed by the plain B3LYP-D3/A-VTZ\* at periodic level of 4390 K (see Fig. 5). Very similar agreement was computed for all considered species as shown in Fig. 6, in which a very good linear correlation is seen between  $BE(ONIAM2)$  and  $BE(DFT)$ . Therefore, we can confidently assume the periodic B3LYP-D3/A-VTZ\* (closed shell molecules) or the M06-2X/A-VTZ\* (radical species) plain  $BE$  values as reliable and accurate enough and are those actually used in this work.

### 3.2.3. $BE$ computed with composite DFT/HF-3c method

In the previous Section we proved the DFT/A-VTZ\* as a reliable and accurate method to compute the  $BE$ s of molecules and radicals on the crystalline (010) P-ice ice slab. However, this approach can become very computational costly when moving from crystalline to amorphous model of the interstellar ice, as larger unit cells are needed to enforce the needed randomness in the water structure. Therefore, we tested the efficiency and accuracy of the cost-effective computational HF-3c method (see § 2).

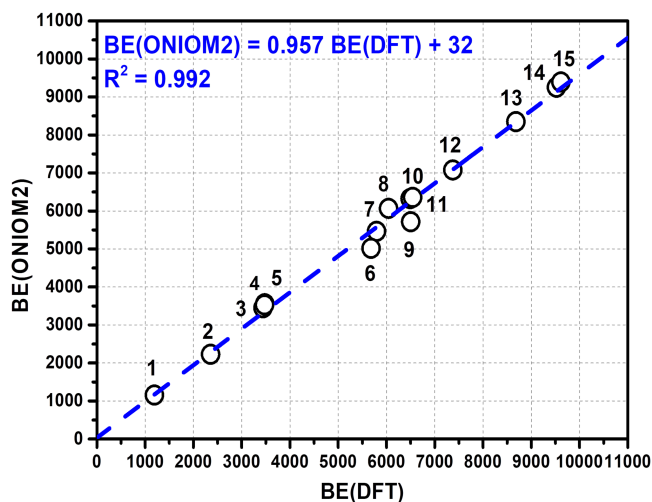


**Figure 6.** Linear fit between periodic DFT/A-VTZ\*  $BE$  values ( $BE(DFT)$ ) and the basis set extrapolated ONIAM2  $BE$  values ( $BE(ONIAM2)$ ). All values are in K. Fit parameters are also reported. Legend: 1: $H_2$ ; 2: $CO$ ; 3: $CO_2$ ; 4: $HCO\bullet$ ; 5: $OCS$ ; 6: $H_2S$ ; 7: $HCN$ ; 8: $NH_2\bullet$ ; 9: $H_2CO$ ; 10: $HCl$ ; 11: $OH\bullet$ ; 12: $NH_3$ ; 13: $CH_3OH$ ; 14: $HCOOH$ ; 15: $HCONH_2$ .

To this end, we adopted a composite procedure which has been recently assessed and extensively tested in the previous work by some of us on the structural and energetic features of molecular crystals, zeolites and biomolecules (Cuttini et al. 2016, 2017, 2019). We started from the DFT/A-VTZ\* optimized structure just discussed for the crystalline ice. We re-optimize each structure at HF-3c level to check the changes in the structures resulting from the more approximated method. Then we run a single point energy calculations at the DFT/A-VTZ\* (B3LYP-D3 and M06-2X) levels to evaluate the final  $BE$  values. The results obtained are summarized in Fig. 7, showing a very good linear correlation between the  $BE$  values computed as described.

The largest percentage differences are found for the smallest  $BE$ s, that is, those dominated by dispersion interactions or very weak quadrupolar interactions (i.e.,  $N_2$ ,  $O_2$ ,  $H_2$  and  $CH_4$ ) in which the deficiencies of the minimal basis set encoded in the HF-3c cannot be entirely recovered by the internal corrections. For higher  $BE$  values, the match significantly improves, in some cases being almost perfect. Even for radicals, the composite approach gives good results. It is worth mentioning that HF-3c optimized geometries are very similar to the DFT-optimized ones (only slight geometry alterations occurred), indicating that the adducts are well-defined minima in both potential energy surfaces. This successful procedure calibrated on crystalline ice is therefore adopted to model the adsorption of all 21 species on the proposed amorphous slab model, a task which would have been very expensive at the full DFT/A-VTZ\* level.

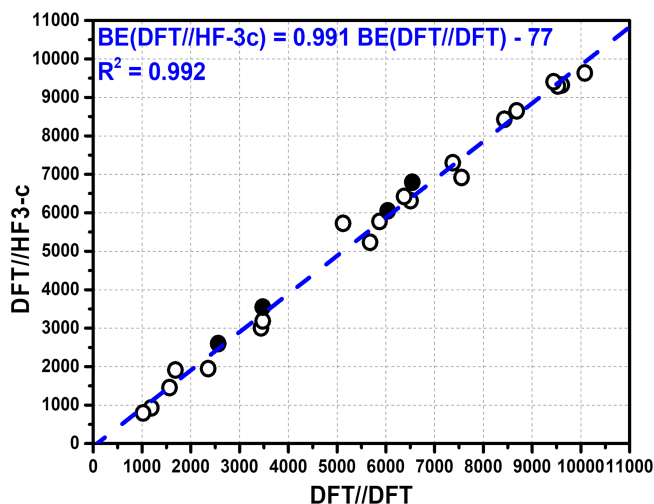


**Figure 7.** Linear fit between the  $BE$  values calculated with the full DFT computational scheme and the  $BE$  values calculated with the composite DFT//HF-3c computational scheme for the crystalline ice model (all values in K). Black-filled and empty triangles stand for open-shell and closed-shell species, respectively.

### 3.3. $BE$ s on amorphous solid water (ASW)

On the ASW model, due to the presence of different binding sites, a single  $BE$  value is not representative of the whole adsorption processes as it is the case for almost all adsorbates on the crystalline surface. Therefore, we computed the  $BE$  with the composite DFT//HF-3c procedure (see § 3.2.3) by sampling different adsorption sites at both the “top” and “bottom” surfaces of the amorphous slab. The starting initial structures of each adsorbate were setup by hand, following the maximum electrostatic complementarity between the EPMS (see Fig. 3) of the ice surface and that of a given adsorbate. For each molecule, at least four  $BE$  values have been computed on different surface sites. Figure 8 reports the examples of methanol and formamide: for each molecule, we show the geometry on the crystalline ice and in two different sites of ASW, as well as the  $BE$  associated with each geometry. For methanol, the  $BE$  is 8648 K in the crystalline ice, whereas it is 4414 and 10091 K in the two shown ASW sites. Similarly, for formamide,  $BE$  is 9285 K on the crystalline ice and 6639 and 8515 K on the ASW. These two examples show that  $BE$ s on ASW can differ more than a twice depending on the site and that the value on the crystalline ice can also be substantially different to that on the ASW.

Figure 9 shows the computed  $BE$ s, on crystalline ice and ASW, for the studied species. The list of all computed  $BE$  values on ASW is reported in Table 2, while Table 3 reports the computed minimum and maximum  $BE$  values on ASW and the  $BE$ s on the crystalline ice for all the studied species. As already mentioned when presenting the methanol and formamide examples, the amorphous nature of the ice can yield large differences in the calculated  $BE$ s with respect to the

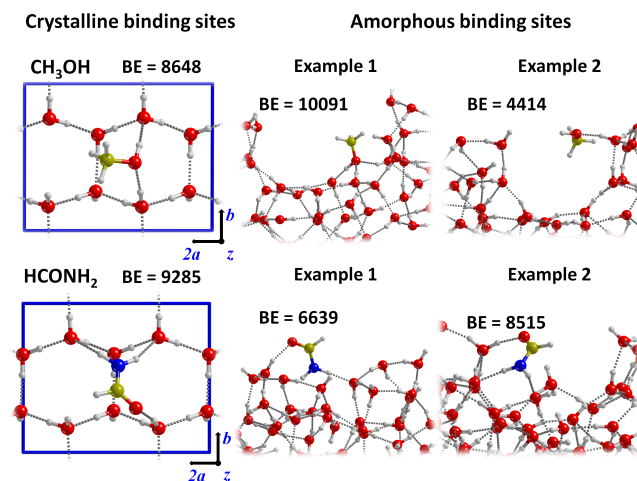


**Figure 8.** Comparison of the final optimized geometries for  $\text{CH}_3\text{OH}$  and  $\text{HCONH}_2$  (as illustrative examples) on the crystalline ice (§ 3.1.1) and on the ASW (§ 3.1.2). The  $BE$  values (in Kelvin) are reported in each plot.

crystalline values. Figure 9 shows that while the  $BE$ s for crystalline *versus* amorphous ices are very close to each other for  $\text{H}_2$ ,  $\text{O}_2$ ,  $\text{N}_2$ ,  $\text{CH}_4$ ,  $\text{CO}$ ,  $\text{CO}_2$ ,  $\text{OCS}$ , the ones computed for the remaining molecules for the crystalline ice fall in the highest range of the distribution of the amorphous  $BE$  values. This behavior can be explained considering the smaller distortion energy cost upon adsorption for the crystalline ice compared to the amorphous one. The different local environment provided by crystalline *versus* amorphous ices is also the reason for  $\text{HCl}$  being molecularly adsorbed at the crystalline ice while becomes dissociated at the amorphous one. Further details about the case of  $\text{HCl}$  are reported in section A.2 of the Appendix. Probably this will not occur for  $\text{HF}$ , not considered here, which is expected to be molecularly adsorbed on both ices due to its higher bond strength compared to  $\text{HCl}$ . Nevertheless, as we did not explore exhaustively all possible configurations of the adsorbates at the amorphous surfaces, we cannot exclude that some even more/less energetic binding cases remain to be discovered.

Some adsorbates show similar trends in the  $BE$ s, despite their different chemical nature. This is shown in Fig. 10, in which we plot the  $BE$  values on ASW for four molecules that have been adsorbed at the same adsorption sites: formaldehyde, formic acid, formamide and methanol. The  $BE$  distributions for the  $\text{H}_2\text{CO}$  and  $\text{HCOOH}$  are very similar (in their relative values), and those for  $\text{CH}_3\text{OH}$  and  $\text{HCONH}_2$  show some similarities, despite the large difference in the chemical functionality.

## 4. DISCUSSION

A first rather expected result of our computations is that the  $BE$  of a species on the ASW is not a single value: depending on the species and the site where it lands, the  $BE$

**Table 1.** Summary of the  $BE$  values (in Kelvin) obtained for the crystalline P-ice (010) slab with DFT//DFT and DFT//HF-3c methods. Legend: “ $BE\ disp$ ” =  $BE$  value including the D3 contribution, “ $BE\ no\ disp$ ” =  $BE$  values not including D3 contribution; “-disp(%)” = absolute (percentage) contribution of dispersive forces to the total  $BE\ disp$ .

Species	(010) P-ice crystalline slab DFT//DFT			(010) P-ice crystalline slab DFT//HF-3c		
	$BE\ disp$	$BE\ no\ disp$	-disp(%)	$BE\ disp$	$BE\ no\ disp$	-disp(%)
H <sub>2</sub>	1191	565	625(53)	926	241	686(74)
O <sub>2</sub>	1022	-373	1034(137)	794	-84	878(110)
N <sub>2</sub>	1564	-72	1636(104)	1455	-180	1636(160)
CH <sub>4</sub>	1684	-229	1912(113)	1912	-349	2261(118)
CO	2357	698	1660(71)	1948	60	1888 (97)
CO <sub>2</sub>	3440	1540	1900(55)	3007	938	2069(69)
OCS	3476	120	3356(97)	3187	265	2923(92)
HCl	6507	4402	2093(32)	6314	3488	2237(39)
HCN	5124	3067	2057(29)	5725	3271	3043(48)
H <sub>2</sub> O	8431	6844	1588(19)	8431	6808	1612(19)
H <sub>2</sub> S	5677	3380	2297(40)	5232	3199	2105(40)
NH <sub>3</sub>	7373	5533	1852(25)	7301	5484	1816(25)
CH <sub>3</sub> CN	7553	4450	3103(41)	6916	3259	2598(44)
CH <sub>3</sub> OH	8684	6014	2670(31)	8648	6026	2237(27)
H <sub>2</sub> CO-SC1	5869	3885	1985(34)	5773	4053	2369(37)
H <sub>2</sub> CO-SC2	6375	3692	2682(42)	6423	3716	2057(36)
HCONH <sub>2</sub> -SC1	9610	6459	3151(33)	9321	6158	3163(34)
HCONH <sub>2</sub> -SC2	10079	6483	3608(36)	9634	6074	3560(37)
HCOOH	9526	7325	2189(23)	9297	7168	2117(23)
HCOOH-SC	9442	7301	2021(21)	9405	7541	1864(20)
OH•	6543*			6795*		
HCO•	3476*			3548*		
CH <sub>3</sub> •	2562*			2598*		
NH <sub>2</sub> •	6038*			6050*		

\*Notes: For radical species (energy at M06-2X level) we cannot discern between  $disp$  and  $no\ disp$  data.

can largely differ, even by more than a factor two (Table 3). This has already discussed in the literature, for instance for H adsorption on both crystalline and amorphous ice models (Ásgeirsson et al. 2017). This has important consequences both when comparing the newly computed  $BEs(\theta)$  with those in the literature § 4.1 and for the astrophysical implications § 4.2. We will discuss these two aspects separately in the next two sections.

#### 4.1. Comparison $BE$ values in literature

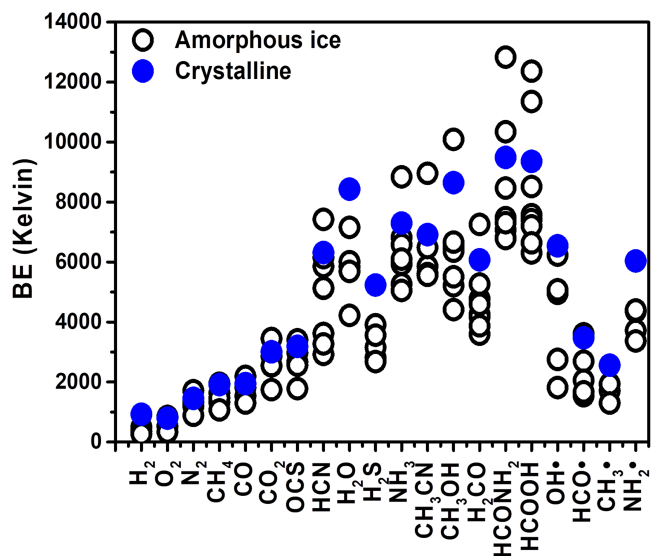
Being such a critical parameter,  $BEs$  have been studied from an experimental and theoretical point of view. In this section, we will compare our newly computed values with those in the literature, separating the discussion for the experimental and theoretical values, respectively. We will then also comment on the values available in the databases that are used in many astrochemical models.

##### 4.1.1. Comparison with experimental values

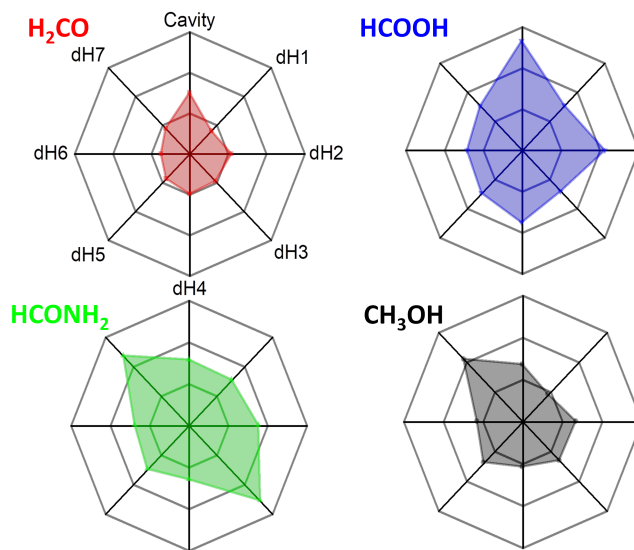
In the present computer simulation we have computed the binding energy ( $BE$ ) released when a species is adsorbed on the surfaces of the ice models (either crystalline or amorphous) at very low adsorbate coverage  $\theta$  ( $\theta \rightarrow 0$ ). The correct comparison with experiments would therefore be with microcalorimetric measurements at the zero-limit adsorbate coverage. In astrochemical laboratories, Temperature Programmed Desorption (TPD) is, instead, the method of choice and is related to the desorption activation energy ( $DAE$ ).  $DAE$  derives indirectly from the TPD peaks through the Redhead’s method (Redhead 1962), or more sophisticated techniques. TPD usually start from an ice surface hosting a whole monolayer of the adsorbate and therefore depends also on  $\theta$  (He et al. 2016), rendering the comparison with the theoretical  $BE$  not straightforward (King 1975). Ice struc-

**Table 2.** *BE* values (K) calculated with DFT//HF-3c method for every case on the amorphous slab model, where the ZPE correction has not been added.

Amorphous ice <i>BE</i> values								
Species	Case 1	Case 2	Case 3	Case 4	Case 5	Case 6	Case 7	Case 8
H <sub>2</sub>	469	505	277	361	265			
O <sub>2</sub>	818	854	854	529	337			
N <sub>2</sub>	1347	1708	1311	1191	890			
CH <sub>4</sub>	1323	1960	1636	1467	1070			
CO	1816	2189	1540	1527	1299			
CO <sub>2</sub>	2863	3452	2538	2550	1744			
OCS	3404	2971	2670	2562	1780			
HCN	2923	5124	3620	5136	3271	5857	6146	7421
H <sub>2</sub> O	7156	5845	6014	5689	4222			
H <sub>2</sub> S	2814	3909	3151	3560	2682			
NH <sub>3</sub>	8840	5268	6820	5930	6579	6098	5052	
CH <sub>3</sub> CN	8960	5857	5617	5557	6483			
CH <sub>3</sub> OH	6531	4414	6519	6362	5208	6663	5509	10091
H <sub>2</sub> CO	3596	4258	4174	4775	5268	4594	3873	7253
HCONH <sub>2</sub>	12833	7481	10344	6820	8467	7072	6783	7313
HCOOH	7577	7409	8515	12364	6302	7204	6639	11354
OH•	6230	1816	4955	2754	5076			
HCO•	2694	2057	1540	3608	1672			
CH <sub>3</sub> •	1708	1936	1299					
NH <sub>2</sub> •	4354	3716	4402	3368				


**Figure 9.** Comparison between the DFT//HF-3c *BE*s (in Kelvin) computed on the crystalline ice (filled blue circles) and ASW (open circles), respectively, for 20 species studied here: HCl is missing as it dissociates on the ASW (see text).

turing processes may also affect the final *DAE*. Sometimes, TPD experiments only provide desorption temperature peaks


**Figure 10.** Spider graphs of the DFT//HF-3c *BE* values (in Kelvin) calculated on the same adsorption eight sites of the ASW for the H<sub>2</sub>CO (red), CH<sub>3</sub>OH (black), HCONH<sub>2</sub> (green) and HCOOH (blue) molecules. The *BE* values scale goes from 0 Kelvin (center of the graph) to 14433 Kelvin (vertices of the polygon) in steps of 4811 Kelvin. Labeling of dH and dO sites is referring to Fig. 3

**Table 3.** Summary of our computed *BEs* and comparison with data from the literature. The first column reports the species, the columns 2 to 4 the *BEs* computed in the present work and corrected for the ZPE, columns 5 and 6 the values obtained via calculations from other authors, column 7 and 8 the values in the two astrochemical databases KIDA and UMIST (see text), and the last columns the values measured in different experiments. Units are in K and the references are listed in the notes below.

Species	BEs from this work			BEs from literature					
	Crystalline ice	ASW		Computed		Databases		Experiments	
	BE(0) <i>disp</i>	Min	Max	Das <sup>(a)</sup>	Wakelam <sup>(b)</sup>	UMIST <sup>(c)</sup>	KIDA <sup>(d)</sup>	Penteado <sup>(e)</sup>	Others
H <sub>2</sub>	790	226	431	545	800	430	440	480 ± 10	322-505 <sup>(f)</sup>
O <sub>2</sub>	677	287	729	1352	1000	1000	1200	914-1161	920-1520 <sup>(f)</sup>
N <sub>2</sub>	1242	760	1458	1161	1100	790	1100	1200	790-1320 <sup>(f1)</sup> 900-1800 <sup>(f1)</sup>
CH <sub>4</sub>	1633	914	1674	2321	800	1090	960	1370	960-1947 <sup>(f,g,h)</sup>
CO	1663	1109	1869	1292	1300	1150	1300	863-1420	870-1600 <sup>(f)</sup> 980-1940 <sup>(f1)</sup>
CO <sub>2</sub>	2568	1489	2948	2352	3100	2990	2600	2236-2346	
OCS	2722	1520	2907	1808	2100	2888	2400	2325**	2430 <sup>(i)</sup>
HCl	5557	(l)	(l)	4104	4800		5172		5172 <sup>(m)</sup>
HCN	6392	2496	6337	2352	3500	2050	3700		
H <sub>2</sub> O	7200	3605	6111	4166	4600	4800	5600	4815-5930	
H <sub>2</sub> S	4468	2291	3338	3232	2500-2900	2743	2700	2296**	
NH <sub>3</sub>	6235	4314	7549	5163	5600	5534	5500	2715**	
CH <sub>3</sub> CN	5906	4745	7652	3786	4300	4680	4680	3790**	
CH <sub>3</sub> OH	7385	3770	8618	4511	4500-5100	4930	5000	3820**	3700-5410 <sup>(n,o,p)</sup>
H <sub>2</sub> CO	5187	3071	6194	3242	5100	2050	4500	3260±60	
HCONH <sub>2</sub>	8104	5793	10960		6300	5556			7460-9380 <sup>(q)</sup>
HCOOH	7991	5382	10559	3483		5000	5570	4532**	
OH•	5588	1551	5321	3183	3300-5300	2850	4600	1656-4760	
HCO•	2968	1315	3081	1857	2300-2700	1600	2400		
CH <sub>3</sub> •	2188	1109	1654	1322	2500	1175	1600		
NH <sub>2</sub> •	5156	2876	4459	3240	2800-4500	3956	3200		

\*Notes: <sup>(a)</sup>(Das et al. 2018); <sup>(b)</sup>Wakelam et al. (2017); <sup>(c)</sup>McElroy et al. (2013); <sup>(d)</sup>Wakelam et al. (2015); <sup>(e)</sup>Penteado et al. (2017); <sup>(f)</sup>He et al. (2016), note that <sup>(f1)</sup> refers to porous ice; <sup>(g)</sup>Raut et al. (2007); <sup>(h)</sup>Smith et al. (2016); <sup>(i)</sup>Ward et al. (2012); <sup>(l)</sup>HCl molecule dissociate; <sup>(m)</sup>Olanrewaju et al. (2011b) <sup>(n)</sup>Minissale et al. (2016) <sup>(o)</sup>Martín-Doménech et al. (2014) <sup>(p)</sup>Bahr et al. (2008) <sup>(q)</sup>Chaabouni et al. (2018) note that the *BE* refers to the silicate substrate because it is larger than that of water ice; \*\* Results estimated from the work of Collings et al. (2004), reported in Table 2 of Penteado et al. (2017)

$T_{des}$ , without working out the *DAE*. This is the case of the fundamental work by Collings et al (Collings et al. 2004). Therefore, *BE* reported in the review by Penteado et al (Penteado et al. 2017) relative to the Collings et al data (see Table 3) were computed through the approximate formula:  $BE(X) = [T_{des}(X)/T_{des}(H_2O)]BE(H_2O)$ , in which  $T_{des}(X)$  is the desorption temperature of the *X* species contrasted with that of water  $T_{des}(H_2O)$  to arrive to the corresponding  $BE(X)$  by assuming that of water to be 4800 K. For the above

reasons, a one-by-one comparison between experiment and modeling is outside the scope of the present paper.

Following the above warnings we can now analyze Table 3 reporting the recent compilation by Penteado et al. (2017) (*vide supra*) plus the values appeared in the literature after that compilation. We start with the cases of two measurements carried out by He et al. (2016) on porous amorphous ice surfaces, for N<sub>2</sub> and CO. Table 3 shows two values, reported by He et al. for the two extreme cases of when the ice

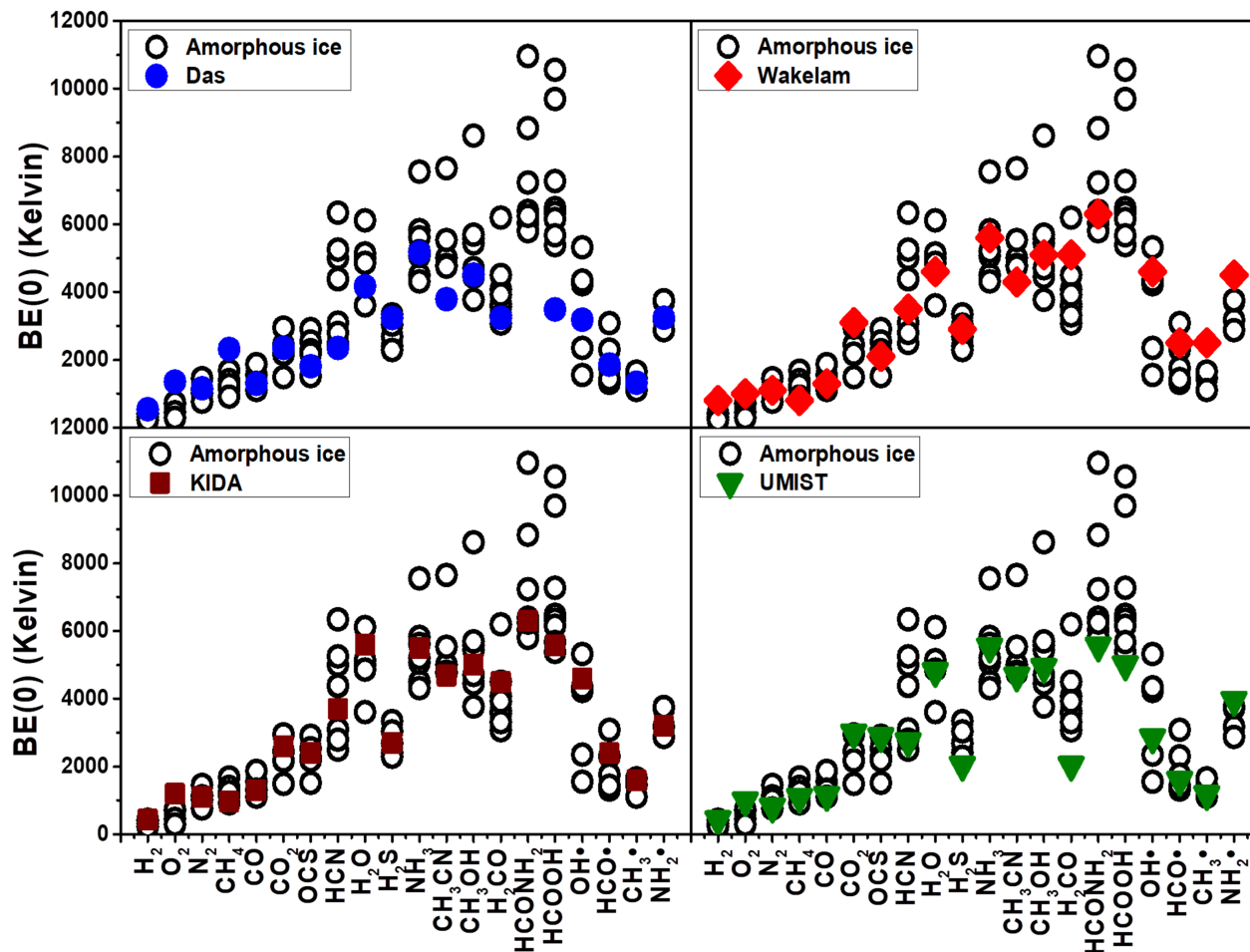


**Figure 11.** Comparison of the computed zero point energy corrected  $BE(0)s$  for the amorphous ice model with respect to those by Das et al., Wakelam et al. and reported in the KIDA and UMIST databases (McElroy et al. 2013; Wakelam et al. 2015, 2017; Das et al. 2018).

is completely covered by the species (the smaller value) and when, on the contrary, it is less than a monolayer (the largest value), which is the one to compare with our computed values. Our  $BE$  on amorphous ice models are in reasonable agreement with that measured by He et al. for CO (1109-1869 K versus 1940 K), and on the lower side for  $N_2$  (760-1455 K versus 1800 K). It is worth-noting that the comparison is much better when referring to the non-porous amorphous ice measurements by the same authors: for CO and  $N_2$  the measured  $BE$  values are 1600 K and 1320 K, indeed well bracketed by our  $BE(0)$ .

Data from Penteadó et al (Penteadó et al. 2017) extracted from the TPD of Collings et al (Collings et al. 2004) for  $NH_3$  adsorbed on ice layer gave a  $BE$  of 2715 K. This value is, however, identical to that from the TPD of  $NH_3$  adsorbed on gold surface (no water ice), proving that that  $BE$  is relative to the  $NH_3/NH_3$  lateral interaction within the adsorbed  $NH_3$  multilayer and not due to the interaction with the ice surface. For reasons explained in Collings et al (Collings et al. 2004)

the  $BE$  of  $NH_3$  on ice is assumed of the same order of that of water, i.e. around 4800 K, in better agreement with the UMIST value of 5500 K (McElroy et al. 2013). Indeed, our data (see Table 3, ZPE corrected) of 4300-7500 K brackets the experimental ones. The computed highest values emphasize the H-bond acceptor capability of  $NH_3$  occurring on few specific sites characterized by very high electrostatic potential, only important for very low  $NH_3$  coverage, not easily accessible in the TPD experiments. For the  $H_2O$  case, the computed  $BE(0)s$  (Table 3) for the amorphous ice are in the 3605-6111 K range, reasonably bracketing the experimental one of 4815-5930 K.

In general, the comparison of our  $BE$  values computed on the ASW with those measured by the various experiments reported in Table 3 shows an excellent agreement, when considering the ranges in our values and the ranges in the values of the experiments. Only one species seems to have a relatively different computed and measured BEs:  $O_2$ . For  $O_2$ , experiments tend to provide larger values with respect to

what we computed (our largest value is 729 K while the lowest measured value is 914 K). For many other species, except  $\text{H}_2$ , our computed lowest  $BEs(0)$  are within the range of the measured ones, but we predict sites where  $BEs(0)$  are larger, which may have important astrophysical implications (§ 4.2). Finally, for  $\text{H}_2$  we predict sites where the  $BE(0)$  is (slightly) lower than the measured ones.

#### 4.1.2. Comparison with computed values

In the literature, there are two works that reported computations of  $BEs$  for a large set of molecules, those by Wakelam et al. (2017) and by Das et al. (2018). The former carried out computations considering only one water molecule whereas the latter considered a cluster of up to six water molecules.

The first aspect to notice is, therefore, that none of these two studies can, by definition, reproduce the strong adsorption sites that we have in our ASW model. Indeed, only the adoption of more realistic and periodically extended ice models allows to fully considering the hydrogen bond cooperativity, which will enhance the strength of the interaction with adsorbates at the terminal dangling hydrogen atoms exposed at the surface. This important effect is entirely missed by the two above mentioned works. It is not surprising, then, that our crystalline and ASW  $BEs$  differ, sometimes substantially, from the Wakelam et al. and Das et al. values (as, by the way, they differ between themselves as well). This is clearly shown in Fig. 11 where we report the comparison of our computed values with those by Wakelam et al. and Das et al., respectively. In general, both work values tend to lay in the low end of our computed  $BEs$ . As extreme examples, our ASW  $BEs$  are larger for  $\text{CH}_3\text{CN}$  and  $\text{HCOOH}$ . The inverse effect is observed for the smallest studied species: our  $BEs$  are smaller than those computed by Wakelam et al. and Das et al. for  $\text{H}_2$  and  $\text{O}_2$ .

#### 4.1.3. Comparison with values in astrochemical databases

Two databases list the  $BE$  of the species used by the astrochemical models: the KIDA (Kinetic Database for Astrochemistry, <http://kida.astrophy.u-bordeaux.fr/>; Wakelam et al. (2015)) and UMIST (<http://udfa.ajmarkwick.net/index.php>; McElroy et al. (2013)). The comparison between our newly computed values and those reported in the two databases is shown in Fig. 11. The general remarks that we wrote for the comparison with the literature experimental and theoretical values (§ 4.1.1 and 4.1.2) roughly apply here: the databases quote  $BE$  values in the low end of ours. This is not surprising, as the databases are compiled based on the experimental and theoretical values in the literature. We just want to emphasize here, once again, that the sites with large binding energies are lacking and this may have important consequences in the astrochemical model predictions.

## 4.2. Astrophysical implications

$BEs$  enter in two hugely important ways in the chemical composition of interstellar objects/clouds: (i) they determine at what dust temperature the frozen species sublimate, and (ii) at what rate the species can diffuse in the ice, as the diffusion energy is a fraction of the  $BE$  species. Both processes are mathematically expressed by an exponential containing the  $BE$ . Therefore, even relatively small variations of the  $BE$  can cause huge differences in the species abundances in the gas phase and on the grain surfaces, where they can react with other species.

In this context, probably the most important astrophysical implication of the present study is that in our ASW model (which is likely the best description to represent the interstellar amorphous ice so far available in the context of the  $BE$  estimates) a species does not have a single value, but a range of values that depend on the species itself and the site where it is bound. The range can spread by more than a factor two: this obviously can have a huge impact on the modeling and, consequently, our understanding of the interstellar chemical evolution.

#### 4.2.1. Impact of multiple $BEs$ in astrochemical modeling

To give a practical example of the impact on the gaseous abundance, we built a toy model for the interstellar ice and simulated the desorption rate of the ice as a function of the temperature. Our scope here is not to compare the toy model predictions with astronomical observations or laboratory experiments: we only mean to show how multiple  $BEs$  (we used the electronic  $BEs$ ) would lead, in principle, to a different behavior of the ice sublimation process. Therefore, we developed a toy model that does not contain diffusion or reaction processes on the ice surface or rearrangement of the ice during the ice heating, but only a layered structure with two species, specifically water and methanol, where molecules have the range of  $BEs$  calculated in section 3. We then show how the multiple  $BEs$  affect the temperature at which peaks of desorption appear, considering that only species at the surface of the ice, namely exposed to the void, can sublimate (and not the entire bulk). In this toy model, we considered ten layers for an icy grain mantle, where the bottom five are made entirely of water and each of the top five layers contains 80% of water and 20% of methanol. The methanol molecules with different  $BEs$  are distributed randomly on each layer, with a same proportion of  $BE$  sites. Looking at the  $BE$  values computed with the DFT//HF-3c method on the ASW model, methanol has eight  $BE$  values (4414, 5208, 5509, 6362, 6519, 6531, 6663 and 10091 K) and, at each layer, there will be 12.5% of methanol molecules with each of the eight  $BEs$ . The same applies for water molecules, for which we have computed five possible  $BEs$  (4222, 5689, 5845, 6014 and 7156 K), with 20% molecule with each  $BE$ . In this model, only molecules of the layers in contact with the void can

evaporate: for example, methanol molecules can be trapped if they have water molecules with larger  $BE$ s on top of them.

We start with an ice temperature of 10 K and at the end it reaches 400 K in  $10^5$  yr, to simulate the heating of a collapsing Solar-like protostar. The plot of the desorption rates is shown in Fig. 12, where we also show them assuming the  $BE$  values from the KIDA database for methanol and water, respectively. First, when only the KIDA values for  $BE$  are assumed, water molecules desorb at about 110 K; methanol has two peaks of desorption rates, the first at about 95 K, corresponding to the desorption of the methanol molecules not trapped by the water molecules, and the second peak at about 110 K, when all water molecules desorb so that no methanol molecules are trapped. Note that the desorption of the water molecules of the bottom layers arrives at a slightly larger temperature.

Not surprising, the introduction of multiple  $BE$ s produces multiple peaks of desorption, both for water and methanol. Figure 12 shows that the water desorption rate has a small peak at  $\sim 75$  K, a larger one at  $\sim 120$  K, then another at  $\sim 140$  K and, finally, a last peak at  $\sim 190$  K. Methanol starts to desorb at 80 K, the bulk is desorbed between 120 and 140 K, and a last peak is seen around 190 K. We emphasize again that this is a toy model meant to show the potential impact of the new  $BE$ s on the astrochemical modeling. The details will depend on the real structure of the water ice and how molecules are distributed on the icy mantles. They will determine how many sites have a certain  $BE$  value and how molecules are trapped in the ice. As a very general remark, we can conclude that species can be in the gas phase at lower and higher dust temperatures than if one only considers a single  $BE$ .

#### 4.2.2. Looking forward: implementation of multiple $BE$ s in astrochemical models

Our toy model introduced in the previous subsection shows the importance of considering multiple  $BE$ s for each species in the astrochemical models to have more realistic predictions. In this work, we provide the possible  $BE$ s for 21 species (Table 3). Very likely, they cover most of the possibilities, as they span a large range of H-bonds within the water molecules of the ASW. However, from a computational standpoint, such an adsorption variability has to be fully explored, in which plotting the different calculated  $BE$ s in histograms is useful to provide insights on the shape of the  $BE$  distribution (Song & Kästner 2017). Moreover, in order to build a reliable astrochemical model one would also need to know the relative probability for each  $BE$  and our present study is unable to provide sensible numbers. For that, a statistical study on an ASW model that is much larger than the one used here is necessary. This is a step that we indeed plan to take in future studies. Meanwhile, we adopted a distribution in which we assign an equal fraction of molecules to each  $BE$ . If one looks carefully at the distribution of the

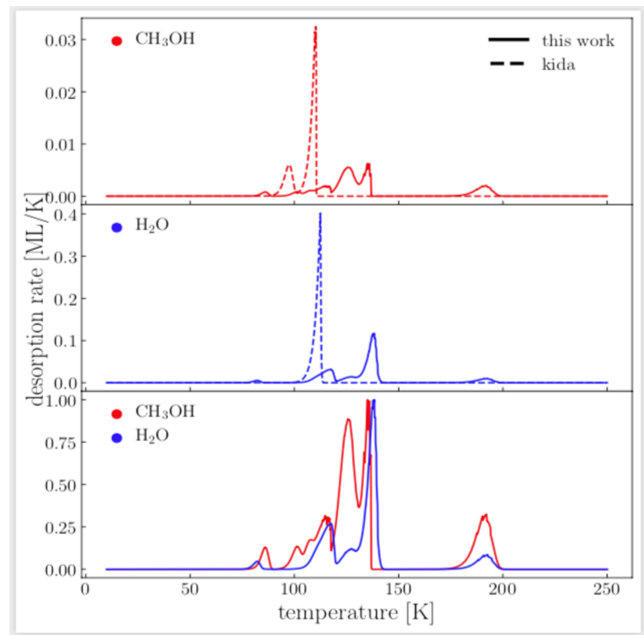


**Figure 12.** Desorption rate of methanol (red curves) and water (blue curves) as a function of the temperature. In these computations, the ice is assumed to be composed by ten layers: the bottom five layers contain water while the top five contain 80% of water and 20% of methanol. The ice is assumed to be at 10 K at the beginning of the simulation and it reaches 400 K in  $10^5$  yr. The curves refer to the case when a single  $BE$  (from the KIDA database) is considered for water and methanol, respectively (dashed line), and when the multiple  $BE$ s of this work are considered (solid line). The bottom panel shows the methanol and water desorption rates normalised to one.

$BE$ s for each molecule, they are not uniformly distributed but peak around some values: for example, methanol has a peak around 6000 K and an extreme value of 10091 K only, so that, very likely, this site will be less populated than the sites around 6000 K, as shown by Figure 10. Yet, considering even a smaller fraction of these extreme values may have important consequences, for example in the so-called snow lines of protoplanetary disks, or even on the observed abundances towards hot cores and hot corinos, or, finally, towards prestellar cores.

#### 4.2.3. Comments on $N_2$ , CO and HCl

Finally, we would like to comment on three species of the studied list,  $N_2$ , CO and the hydrogen chloride (HCl).

$N_2$  and CO: Our computations show that the  $BE$  of CO is definitively larger than that of  $N_2$ , against the values that are in the astrochemical databases (see Table 3): on average, our computed  $BE$ s differ by about 400 K whereas in the data bases the difference is 200 and 360 K in KIDA and UMIST, respectively. This difference very likely can explain why observations detect  $N_2H^+$ , which is formed in the gas phase from  $N_2$ , where CO is already frozen on the grain mantles

(e.g. Bergin et al. 2002; Tafalla et al. 2004; Redaelli et al. 2019), a debate which has been going on for almost two decades (e.g. Öberg et al. 2009; Pagani et al. 2012).

In order to quantify the effect a specifically focused modeling will be necessary, which is out of the scope of the present work. Here we want just to alert that the new *BEs* might explain some long-standing mysteries. Another comment regards the difference in the *BEs* on crystalline surfaces and ASW. Again the CO binding energy is about 500 K larger than that of N<sub>2</sub>, and both are larger by about 300 K than those on the ASW, a difference that also has an impact on the snow lines of these two species in protoplanetary disks, where crystalline water ices have been detected (Terada & Tokunaga 2012).

*HCl*: Astrochemical models predict that HCl is the reservoir of Cl in molecular gas (e.g. Schilke et al. 1995; Neufeld & Wolfire 2009; Acharyya & Herbst 2017). However, all the observations so far carried out have found that only a tiny fraction of Cl is in the gaseous HCl, even in sources where all the grain mantles are supposed to be completely sublimated (Peng et al. 2010; Codella et al. 2011; Kama et al. 2015). One possible explanation is that HCl, once formed in the gas phase, is adsorbed on the grain icy mantles and dissociates, as shown by our calculations on the ASW model and also by previous calculations on the crystalline P-ice model (Casassa 2000) and for more sophisticated proton-disordered crystalline ice models (Svanberg et al. 2000). It is a matter to be studied whether the sublimation of the water, when the dust reaches about 100-120 K, would also provide a reactive channel transforming the Cl anion in the neutral atom, this latter obviously unobservable. This would help solving the mystery of HCl not being observed in gas-phase. Furthermore, if that would be the case, the population of the chemically reactive atomic Cl will be increased, with important role in the gas-phase chemistry (see e.g. Balucani et al. 2015; Skouteris et al. 2018).

## 5. CONCLUSIONS

In this work, we present both a new computational approach and realistic models for crystalline and amorphous water ice to be used to address an important topic in Astrochemistry: the binding energies (*BEs*) of molecules on interstellar ice surfaces. We simulated such surfaces by means of two (antipodal) models, in both cases adopting a periodic approach: a crystalline and an amorphous 2D slab models. We relied on density functional theory (DFT) calculations, using the B3LYP-D3 and M06-2X widely used functionals. This approach was further validated by an ONIOM-like correction at CCSD(T) level. Results from this combined procedure confirm the validity of the *BEs* computed with the adopted DFT functionals. The reliability of a cost-effective HF-3c method adopted to optimize the structures at the amor-

phous ice surface sites was proved by comparing the binding energies computed at the crystalline ice surface at DFT//DFT and DFT//HF-3c level, which were found in very good agreement.

On both ice surface models, we simulated the structure and adsorption energetic features of 21 molecules, including 4 radicals, representative of the most abundant species of the dense ISM. A main conclusion is that the crystalline surfaces only show very limited variability in the adsorption sites, whereas the amorphous surfaces provide a wide variety of adsorption binding sites, resulting in a distribution of the computed *BE*. Furthermore, *BE* values at crystalline ice surface are in general higher than those computed at the amorphous ice surfaces. This is largely due to the smaller geometry relaxation cost upon adsorption compared to the amorphous cases, imposed by the tighter network of interactions of the denser crystalline ice over the amorphous ice.

Finally, the *BEs* obtained by the present computations were compared with literature data, both from experimental and computational works, as well as those on the public astrochemical databases KIDA and UMIST. In general, our *BEs* agree relatively well with those measured in laboratory, with the exception of O<sub>2</sub> and, at less extent, H<sub>2</sub>. On the contrary, previous computations of *BEs*, which considered a very small ( $\leq 6$ ) water molecules, provide generally lower values with respect to our new computations and, with no surprise, miss the fact that *BEs* have a spread of values which depend on the position of the molecule on the ice. Since the two astrochemical databases mentioned above are based on the literature data, our *BEs* differ, sometimes substantially, from those quoted and do not report multiple *BEs* values.

We discussed some astrophysical implications, showing that the multiple computed *BEs* give rise to a complex process of interstellar iced mantles desorption, with multiple peaks as a function of the temperature that depends (also) on the ice structure. Our new computations do not allow to estimate how the *BEs* are distributed for each molecule as only a statistical study is necessary for that. The new (multiple) *BEs* of N<sub>2</sub> and CO might explain why N<sub>2</sub>H<sup>+</sup> deplete later than CO in prestellar cores, while the relatively low abundance of HCl, observed in protostellar sources, could be due to the fact that it dissociates into the water ice, as shown by our calculations.

Finally, the present study shows the importance of theoretical calculations of *BEs* on as realistic as possible ice surfaces. This first study of 21 molecules needs to be extended to the hundreds molecules that are included in the astrochemical models to have a better understanding of the astrochemical evolution of the ISM.

## ACKNOWLEDGMENTS

A part of the computational results were from the SF Master thesis "Ab initio quantum mechanical study of the interaction of astrochemical relevant molecules with interstellar ice models", Dipartimento di Chimica, University of Torino, Torino, 2018. SF, LZ and PU acknowledge financial support from the Italian MIUR (Ministero dell'Istruzione, dell'Università e della Ricerca) and from Scuola Normale Superiore (project PRIN 2015, STARS in the CAOS - Simulation Tools for Astrochemical Reactivity and Spectroscopy in the Cyberinfrastructure for Astrochemical Organic Species, cod. 2015F59J3R). The Italian CINECA consortium is also acknowledged for the provision of supercomputing time for part of this project. AR is indebted to the "Ramón y Cajal" program. MINECO (project CTQ2017-89132-P) and DIUE (project 2017SGR1323) are acknowledged. This project has received funding from the European Union's Horizon 2020 research and innovation programme under the Marie Skłodowska-Curie grant agreement No 811312 for the project "Astro-Chemical Origins" (ACO) and from the European Research Council (ERC) under the European Union's Horizon 2020 research and innovation programme, for the Project "The Dawn of Organic Chemistry" (DOC), grant agreement No 741002. Finally, we wish to acknowledge the extremely useful discussions with Prof. Gretobape.

## REFERENCES

- Acharyya, K., & Herbst, E. 2017, ApJ, 850, 105
- Al-Halabi, A., & Van Dishoeck, E. 2007, MNRAS, 382, 1648
- Ásgeirsson, V., Jónsson, H., & Wikfeldt, K. 2017, The Journal of Physical Chemistry C, 121, 1648
- Bahr, S., Toubin, C., & Kempter, V. 2008, The Journal of chemical physics, 128, 134712
- Balucani, N., Ceccarelli, C., & Taquet, V. 2015, MNRAS: Letters, 449, L16
- Bartlett, R. J., & Musiał, M. 2007, Rev Mod Phys, 79, 291
- Becke, A. D. 1988, J Chem Phys, 88, 2547
- . 1993, The Journal of Chemical Physics, 98, 1372
- Bennett, C. J., & Kaiser, R. I. 2007, ApJ, 661, 899
- Bergin, E. A., Alves, J., Huard, T., & Lada, C. J. 2002, ApJ, 570, L101
- Boogert, A. A., Gerakines, P. A., & Whittet, D. C. 2015, Annu Rev Astron Astrophys, 53, 541
- Borden, W. T., Hoffmann, R., Stuyver, T., & Chen, B. 2017, JACS, 139, 9010
- Boys, S. F., & Bernardi, F. 1970, Mol Phys, 19, 553
- Broyden, C. G. 1970, IMA J Appl Math, 6, 76
- Casassa, S. 2000, Chem Phys Lett, 321, 1
- Casassa, S., Ugliengo, P., & Pisani, C. 1997, J Chem Phys, 106, 8030
- Chaabouni, H., Diana, S., Nguyen, T., & Dulieu, F. 2018, A&A, 612, A47
- Codella, C., Ceccarelli, C., Bottinelli, S., et al. 2011, ApJ, 744, 164
- Collings, M. P., Anderson, M. A., Chen, R., et al. 2004, MNRAS, 354, 1133
- Cramer, C. 2002, Essentials of computational chemistry (England, Wiley
- Cuppen, H., Walsh, C., Lamberts, T., et al. 2017, SSRv, 212, 1
- Cutini, M., Civalieri, B., Corno, M., et al. 2016, JCTC, 12, 3340
- Cutini, M., Civalieri, B., & Ugliengo, P. 2019, ACS omega, 4, 1838
- Cutini, M., Corno, M., & Ugliengo, P. 2017, JCTC, 13, 370
- Dapprich, S., Komáromi, I., Byun, K. S., Morokuma, K., & Frisch, M. J. 1999, J Mol Struct:THEOCHEM, 461, 1
- Das, A., Sil, M., Gorai, P., Chakrabarti, S. K., & Loison, J.-C. 2018, ApJS, 237, 9
- Davidson, E. R., & Feller, D. 1986, Chem Rev, 86, 681
- Dohnalek, Z., Kimmel, G. A., Joyce, S. A., et al. 2001, J Phys Chem B, 105, 3747

- Douglas, A., & Herzberg, G. 1942, *Canadian Journal of Research*, 20, 71
- Dovesi, R., Erba, A., Orlando, R., et al. 2018, *Wiley Interdiscip Rev Comput Mol Sci*, 8, e1360
- Dulieu, F., Amiaud, L., Congiu, E., et al. 2010, *A&A*, 512, A30
- Dulieu, F., Congiu, E., Noble, J., et al. 2013, *Sci Rep*, 3, 1338
- Dunning Jr, T. H. 1989, *J Chem Phys*, 90, 1007
- Enrique-Romero, J., Rimola, A., Ceccarelli, C., et al. 2019, *ACS Earth Space Chem*, 3, 2158
- Enrique-Romero, J., Álvarez-Barcia, S., Kolb, F., et al. 2020, *MNRAS*, 493, 2523
- Fayolle, E. C., Balfe, J., Loomis, R., et al. 2016, *ApJL*, 816, L28
- Fletcher, R. 1970, *Comput J*, 13, 317
- Frisch, M., Trucks, G., Schlegel, H., et al. 2009, Inc., Wallingford CT, 121, 150
- Goldfarb, D. 1970, *Math Comput*, 24, 23
- Grimme, S., Antony, J., Ehrlich, S., & Krieg, H. 2010, *J Chem Phys*, 132, 154104
- Grimme, S., Ehrlich, S., & Goerigk, L. 2011, *J Comput Chem*, 32, 1456
- He, J., Acharyya, K., & Vidali, G. 2016, *ApJ*, 825, 89
- Hiraoka, K., Miyagoshi, T., Takayama, T., Yamamoto, K., & Kihara, Y. 1998, *ApJ*, 498, 710
- Hohenberg, P., & Kohn, W. 1964, *Phys Rev*, 136, B864
- Hollenbach, D., & Salpeter, E. 1971, *ApJ*, 163, 155
- Horn, A. B., Chesters, M. A., S, M. M. R., & Sodeau, J. R. 1992, *Journal of Chemical Society Faraday Transaction*, 88, 1077
- Jansen, H., & Ros, P. 1969, *Chem Phys Lett*, 3, 140
- Jones, A. 2013, *A&A*, 555, A39
- Jones, A., Köhler, M., Ysard, N., Bocchio, M., & Verstraete, L. 2017, *A&A*, 602, A46
- Kama, M., Caux, E., López-Sepulcre, A., et al. 2015, *A&A*, 574, A107
- Karssemeijer, L., & Cuppen, H. 2014, *A&A*, 569, A107
- Karssemeijer, L., de Wijs, G., & Cuppen, H. 2014, *PCCP*, 16, 15630
- King, D. A. 1975, *Surface Science*, 47, 384
- Kraus, P., & Frank, I. 2018, *J Phys Chem A*, 122, 4894
- Lee, C., Yang, W., & Parr, R. G. 1988, *Phys Rev B*, 37, 785
- Liu, B., & McLean, A. 1973, *J Chem Phys*, 59, 4557
- Martín-Doménech, R., Caro, G. M., Bueno, J., & Goesmann, F. 2014, *Astronomy & Astrophysics*, 564, A8
- McElroy, D., Walsh, C., Markwick, A., et al. 2013, *A&A*, 550, A36
- McGuire, B. A. 2018, *ApJS*, 239, 17
- McKellar, A. 1940, *Publications of the Astronomical Society of the Pacific*, 52, 187
- Minissale, M., Dulieu, F., Cazaux, S., & Hocuk, S. 2016, *Astronomy & Astrophysics*, 585, A24
- Neufeld, D. A., & Wolfire, M. G. 2009, *ApJ*, 706, 1594
- Noble, J., Congiu, E., Dulieu, F., & Fraser, H. 2012, *MNRAS*, 421, 768
- Novoa, J., & Sosa, C. 1995, *The Journal of Physical Chemistry*, 99, 15837
- Oba, Y., Miyauchi, N., Hidaka, H., et al. 2009, *ApJ*, 701, 464
- Oba, Y., Watanabe, N., Hama, T., et al. 2012, *ApJ*, 749, 67
- Öberg, K. I., van Dishoeck, E. F., & Linnartz, H. 2009, *A&A*, 496, 281
- Olanrewaju, B. O., Herring-Captain, J., A, G. G., Aleksandrov, A., & M, O. T. 2011a, *The Journal of Physical Chemistry A*, 115, 5936
- Olanrewaju, B. O., Herring-Captain, J., Grieves, G. A., Aleksandrov, A., & Orlando, T. M. 2011b, *The Journal of Physical Chemistry A*, 115, 5936
- Pack, J. D., & Monkhorst, H. J. 1977, *Phys Rev B*, 16, 1748
- Pagani, L., Bourgoïn, A., & Lique, F. 2012, *A&A*, 548, L4
- Pantaleone, S., Enrique-Romero, J., Ceccarelli, C., et al. 2020, *Chemical desorption versus energy dissipation: insights from ab-initio molecular dynamics of HCO formation*, , arXiv:2004.11758
- Papajak, E., Zheng, J., Xu, X., Leverentz, H. R., & Truhlar, D. G. 2011, *JCTC*, 7, 3027
- Pascale, F., Zicovich-Wilson, C. M., Lopez Gejo, F., et al. 2004, *J Comput Chem*, 25, 888
- Peng, R., Yoshida, H., Chamberlin, R. A., et al. 2010, *ApJ*, 723, 218
- Penteado, E., Walsh, C., & Cuppen, H. 2017, *ApJ*, 844, 71
- Pople, J. A., Gill, P. M., & Handy, N. C. 1995, *Int J Quantum Chem*, 56, 303
- Raut, U., Famá, M., Teolis, B., & Baragiola, R. 2007, *The Journal of chemical physics*, 127, 204713
- Redaelli, E., Bizzocchi, L., Caselli, P., et al. 2019, *A&A*, 629, A15
- Redhead, P. A. 1962, *Vacuum*, 12, 203
- Rimola, A., Civalleri, B., & Ugliengo, P. 2008, *Langmuir*, 24, 14027
- Rimola, A., Skouteris, D., Balucani, N., et al. 2018, *ACS Earth Space Chem*, 2, 720
- Rimola, A., Taquet, V., Ugliengo, P., Balucani, N., & Ceccarelli, C. 2014, *A&A*, 572, A70
- Schäfer, A., Horn, H., & Ahlrichs, R. 1992, *J Chem Phys*, 97, 2571
- Schilke, P., Phillips, T., & Wang, N. 1995, *ApJ*, 441, 334
- Senevirathne, B., Andersson, S., Dulieu, F., & Nyman, G. 2017, *Mol Astrophys*, 6, 59
- Shanno, D. F. 1970, *Math Comput*, 24, 647
- Shimonishi, T., Nakatani, N., Furuya, K., & Hama, T. 2018, *ApJ*, 855, 27
- Skouteris, D., Balucani, N., Ceccarelli, C., et al. 2018, *ApJ*, 854, 135
- Smith, R. S., May, R. A., & Kay, B. D. 2016, *The Journal of Physical Chemistry B*, 120, 1979

- Song, L., & Kästner, J. 2017, *ApJ*, 850, 118
- Sorrell, W. H. 2001, *ApJL*, 555, L129
- Sure, R., & Grimme, S. 2013, *J Comput Chem*, 34, 1672
- Svanberg, M., Pettersson, J. B. C., & K, B. 2000, *The Journal of Physical Chemistry A*, 104, 5787
- Swings, P., & Rosenfeld, L. 1937, *ApJ*, 86, 483
- Tafalla, M., Myers, P. C., Caselli, P., & Walmsley, C. M. 2004, *A&A*, 416, 191
- Tasker, P. 1979, *Journal of Physics C: Solid State Physics*, 12, 4977
- Tatewaki, H., & Huzinaga, S. 1980, *J Comput Chem*, 1, 205
- Tentscher, P. R., & Arey, J. S. 2013, *JCTC*, 9, 1568
- Terada, H., & Tokunaga, A. T. 2012, *ApJ*, 753, 19
- Tosoni, S., Pascale, F., Ugliengo, P., et al. 2005, *Mol Phys*, 103, 2549
- Ugliengo, P., & Damin, A. 2002, *Chem Phys Lett*, 366, 683
- Wakelam, V., Loison, J.-C., Mereau, R., & Ruaud, M. 2017, *Mol Astrophys*, 6, 22
- Wakelam, V., Loison, J.-C., Herbst, E., et al. 2015, *ApJS*, 217, 20
- Ward, M. D., Hogg, I. A., & Price, S. D. 2012, *Monthly Notices of the Royal Astronomical Society*, 425, 1264
- Watanabe, N., & Kouchi, A. 2002, *ApJL*, 571, L173
- . 2008, *Prog Surf Sci*, 83, 439
- Zamirri, L., Casassa, S., Rimola, A., et al. 2018, *MNRAS*, 480, 1427
- Zamirri, L., Corno, M., Rimola, A., & Ugliengo, P. 2017, *ACS Earth Space Chem*, 1, 384
- Zamirri, L., Pantaleone, S., & Ugliengo, P. 2019a, *J Chem Phys*, 150, 064702
- Zamirri, L., Ugliengo, P., Ceccarelli, C., & Rimola, A. 2019b, *ACS Earth Space Chem*, 3, 1499
- Zhao, Y., & Truhlar, D. G. 2008, *Theor Chem Acc*, 120, 215
- Zicovich-Wilson, C., Pascale, F., Roetti, C., et al. 2004, *J Comput Chem*, 25, 1873

## APPENDIX

## A. COMPUTATIONAL DETAILS

In CRYSTAL17, the multielectron wavefunction is built as a Slater determinant of crystalline/molecular orbitals which are linear combinations of localized functions on the different atoms of the structure which are called Atomic Orbitals (AOs). In a similar manner, the AOs are constructed by linear combinations of localized Gaussian functions which form a basis set. The basis set employed for this work is an Ahlrichs-TVZ (Schäfer et al. 1992), added with polarization functions.

## A.1. Binding energies, Counterpoise and zero point energy corrections

In a periodic treatment of surface adsorption phenomena one of the most relevant energy value, useful to describe the interacting system, is the binding energy  $BE$ s which is related to the interaction energy  $\Delta E$ , so that:

$$BE = -\Delta E \quad (A1)$$

The binding energy per unit cell per adsorbate molecule  $BE$  is a positive quantity (for a bounded adsorbate) defined as:

$$BE = [E_m(M//M) + E(S//S)] - E(SM//SM) \quad (A2)$$

where  $E(SM//SM)$  is the energy of a fully relaxed unitary cell containing the surface slab  $S$  in interaction with the adsorbate molecules  $M$ ,  $E(S//S)$  is the energy of a fully relaxed unitary cell containing the slab alone and  $E_m(M//M)$  is the molecular energy of the free fully optimized adsorbate molecule (the symbol following the double slash identifies the geometry at which the energy is

$$BE = BE^* - \delta E_S - \delta E_M \quad (A3)$$

$$\delta E_S = E(S//SM) - E(S//S) \quad (A4)$$

$$\delta E_M = E(M//SM) - E_m(M//M) \quad (A5)$$

$$BE^* = [E(S//SM) + E(M//SM)] - E(SM//SM) \quad (A6)$$

in which  $\delta E_S$  is the deformation energy of the surface ( $\delta E_S > 0$ ) whereas  $\delta E_M (= \Delta E_M + \Delta E_L)$  counts both the deformation energy of the molecule ( $\Delta E_M$ ) and the lateral intermolecular interactions ( $\Delta E_L$ ) between the infinite molecule images in the same spatial configuration occurring in the  $SM$  periodic system. The purely molecule's deformation energy can be computed as:

$$\Delta E_M = E_m(M//SM) - E_m(M//M) \quad (A7)$$

in which  $E_m(M//SM)$  is the molecular energy of the molecule frozen at the geometry occurring on the surface and  $E_m(M//M)$  is the molecular energy of a fully optimized free molecule, so that  $\Delta E_M > 0$ . The lateral intermolecular interactions,  $\Delta E_L$  are defined as:

$$\Delta E_L = E(M//SM) - E_m(M//SM) \quad (A8)$$

and can be either positive (repulsion) or negative (attraction). With those positions, the  $BE^*$  interaction energy is then deformation and lateral interactions free, being the result of energy differences between periodic calculations carried out at the geometry of the  $SM$  system. For instance,  $E(M//SM)$  is the energy of the unit cell of a crystal containing only a molecule in the same geometry assumed in the  $SM$  system. The above  $BE$  definition can be easily recast to include the basis set superposition error ( $BSSE$ ) correction, using the same counterpoise method adopted for intermolecular complexes (Boys & Bernardi 1970; Davidson & Feller 1986). The definition of the  $BSSE$  corrected interaction energy  $BE^C$  is then:

$$BE^C = BE^{*C} - \delta E_S - \Delta E_M - \Delta E_L^C \quad (A9)$$

$$BE^{*C} = [E(S[M]//SM) + E([S]M//SM)] - E(SM//SM) \quad (A10)$$

$$BSSE = BE - BE^C \quad (A11)$$

in which  $E(S[M]//SM)$  and  $E([S]M//SM)$  are the energy of the slab plus the ghost functions of the molecules and the energy of the infinite replica of molecules with the ghost functions of the underneath slab, respectively. Because the variational theorem ensures that  $BE^{*C} < BE^*$  it immediately results that  $BSSE > 0$ .

Each of the terms of equation A2 can be corrected by the zero point vibrational contribution (in the harmonic approximation),  $ZPE$ , therefore arriving to the definition of the zero point correct binding energy  $BE(0)$  as:

$$BE(0) = [E_m(M//M) + E(S//S)] - E(SM//SM) + [ZPE(M) + ZPE(S) - ZPE(SM)] \quad (A12)$$

$$BE(0) = BE - \Delta ZPE \quad (A13)$$

$$\Delta ZPE = ZPE(SM) - ZPE(M) - ZPE(S) \quad (A14)$$

In this work the  $\Delta ZPE$  has been evaluated for the crystalline ice cases only and the same correction was adopted also to correct the  $BE$  for the the amorphous ice model for the reason described in the Computational Details section.

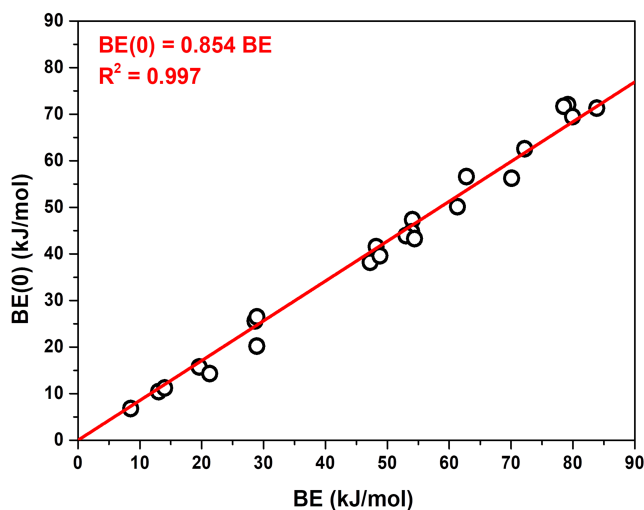


**Figure 13.** Linear regression between  $BE$  and  $BE(0)$  (zero point corrected) values computed for the considered adsorbates on the crystalline ice

#### A.2. Details on HCl adsorbed on crystalline and amorphous ices

Our calculations showed that HCl remains molecularly adsorbed at the crystalline ice surface. At the amorphous one it spontaneously deprotonates making a locally stable ion-pair ( $\text{Cl}^-/\text{H}_3\text{O}^+$ ) (see the figure below). The reason is that for the surface selected to represent the crystalline ice, the ion pair cannot be stabilized by a large enough network of H-bonds due to the rigidity of the structure. On the contrary, at amorphous surface,  $\text{Cl}^-$  is engaged in three H-bonds while the hydronium ion remains embedded in the H-bonds provided by the ice surface. A good solvation of the ion-pair is the key determining the final fate of HCl at the ice surfaces (molecular or ion pair) as already pointed out many years ago by Novoa and Sosa for a small water cluster hosting HCl (Novoa & Sosa 1995). While deprotonation of HCl cannot be excluded for specific crystalline ice surface sites as simulated by Svanberg *et al* (Svanberg *et al.* 2000) when enough dangling hydrogen can stabilize the anion, deprotonation would be much more common at amorphous ice surface or locally distorted crystalline ones, due to the presence of favorable local environment (see Figure 14). Dissociative adsorption was early found by Horn *et al* (Horn *et al.* 1992) through RAIRS spectroscopy of DCl adsorption on thin  $\text{D}_2\text{O}$  film, and by Olanrewaju *et al* (Olanrewaju *et al.* 2011a) through thermal and electron-stimulated desorption experiments.

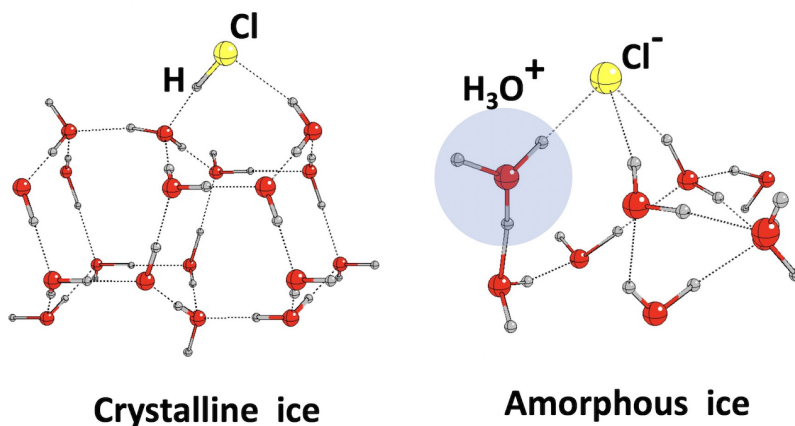


**Figure 14.** Enlarged views of HCl adsorbed on a crystalline and amorphous ice models

### A.3. *CRYSTAL17 computational parameters*

In order to optimize the values of the shrinking factor, the tolerances on integrals of the integration grid (SHRINK, TOLINTEG and GRID parameters (Dovesi et al. 2018) in the code) as described in §2 of the article,  $\text{NH}_3$  has been adopted as a test case. Geometry optimizations for the adsorption process on the crystalline slab model have been run with the previously described computational scheme, varying one-by-one the aforementioned parameters, with convergence on the pure  $\Delta E$  as define by Equation (A1) being the threshold. For this benchmark calculations, *BSE*, distortion and lateral interaction contributions have not been computed. Results are resumed in what follows.

**Table 4.** Optimization of the SHRINK parameter. Tolerances of integrals (TOLINTEG) and integration grid (XLGRID) are fixed to default values.

SHRINK	$k$ points in BZ	$\Delta E$ (K)
2 2	4	7873
3 3	5	7889
4 4	10	7889
5 5	13	7890
6 6	20	7890
7 7	25	7890
8 8	34	7890

From Table 4 it is clear that  $\Delta E$  is practically unaffected by the SHRINK value, thus SHRINK = (2 2) has been used for all calculations, allowing the saving of computational time.

**Table 5.** Optimization of the TOLINTEG parameter (SHRINK = 2 2 and XLGRID).

TOLINTEG	$\Delta E$ (K)
6 6 6 6 12	7889
7 7 7 7 14	7906
8 8 8 8 16	8063
9 9 9 9 18	7981
10 10 10 10 20	7890

As for the SHRINK parameter, the variations of TOLINTEG values does not practically affect the final  $\Delta E$  value. Consequently, its values have been set equal to 7, 7, 7, 7, and 14.

**Table 6.** Optimization of the integration grid parameter (SHRINK = 2 2 and TOLINTEG = 7 7 7 7 14).

GRID	$\Delta E$ (K)
XLGRID	7951
XXLGRID	7951

Again, the  $\Delta E$  is practically unaffected by the changing the adopted grid, therefore XLGRID was selected for all the remaining calculations. Resuming, every other calculation has been carried out with SHRINK = (2 2), TOLINTEG = (7 7 7 7 14) and XLGRID as computational parameters.

#### A.4. Description of dispersive forces

We optimized the geometry of two parallel benzene rings which interact with each other just because of dispersive forces given the apolar nature of the molecule. The results of Figure 15 clearly show that the B3LYP functional needs some a posteriori correction (like the Grimme's D3) for dispersive forces in order to describe correctly the interaction (Grimme et al. 2010), whereas the M06-2X functional is able to describe it correctly without any a posteriori correction (Zhao & Truhlar 2008).

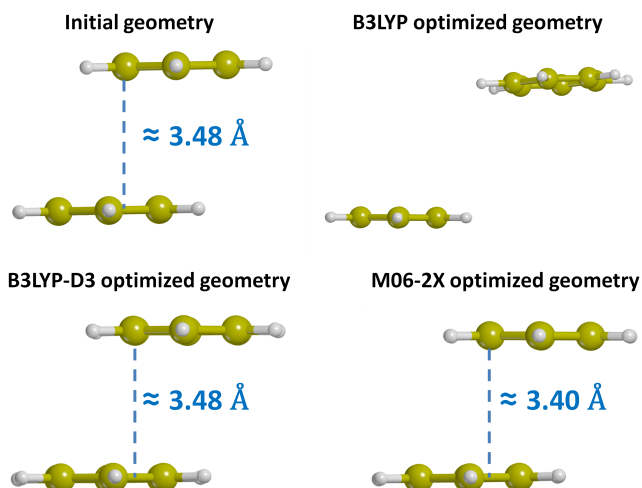


**Figure 15.** Initial and optimized geometry of two parallel benzene rings obtained with B3LYP (without dispersion corrections), B3LYP-D3 and M06-2X functionals. Distances between the planes of the two rings are reported in Angstrom.

#### A.5. ONIOM2 correction

Hereafter we summarize the single components (namely  $BE(\text{CCSD(T)}, \mu\text{-2H}_2\text{O})$  extrapolated,  $BE(\text{DFT}, \mu\text{-2H}_2\text{O})$ ,  $BE(\text{DFT}, \text{ice})$  and finally the corrected  $BE(\text{ONIOM2})$ ) of the ONIOM2 correction done with the extrapolation procedure already described in § 2.

**Table 7.** Summary of the components used for the calculation of the ONIOM2 correction to the  $BE$ s. The last column shows the absolute value of the difference between the  $BE(\text{DFT}, \mu\text{-}2\text{H}_2\text{O})$  value and the corrected  $BE(\text{ONIOM2})$ .

Species	$BE(\text{CCSD(T)}, \mu\text{-}n\text{H}_2\text{O})$ extrapolated	$BE(\text{DFT}, \mu\text{-}n\text{H}_2\text{O})$	$BE(\text{DFT, ice})$	$BE(\text{ONIOM2})$	Diff
H <sub>2</sub>	843	796	1192	1240	47
CO	1127	1165	2356	2318	38
CO <sub>2</sub>	1939	1817	3442	3564	121
OCS	1354	1138	3478	3695	216
H <sub>2</sub> S	2443	2875	5679	5248	432
HCN	3300	3453	5795	5642	153
H <sub>2</sub> CO	3199	3114	6490	6575	85
HCl	3993	4475	6501	6019	482
NH <sub>3</sub>	4246	4389	7376	7233	143
CH <sub>3</sub> OH	5196	5275	8681	8602	79
HCOOH	6263	6223	9522	9562	40
HCONH <sub>2</sub>	5080	5056	9614	9638	24
OH•	4492	4502	6542	6532	10
NH <sub>2</sub> •	3021	2788	6043	6276	233
HCO•	2339	2088	3474	3725	251

## B. CRYSTALLINE ADSORPTION GEOMETRIES

The final optimized structures, together with  $BE$ s and structural properties for every molecule in our set are presented in this section. For some notable cases, more than one initial structure has been modeled. All energetic quantities are in Kelvin (K), while distances are in Å. For every molecule, the gas phase optimized geometry together with its ESP map are also present. In the latter, the isovalue for the electron density is set equal to  $1 \times 10^{-6}$  au, while the values for the ESP (again in au) vary case by case and thus are reported close to the RGB scale legend.

### Fig. Set 16. Adsorption on crystalline ice

”The complete figure set (24 images) is available in the online journal”.

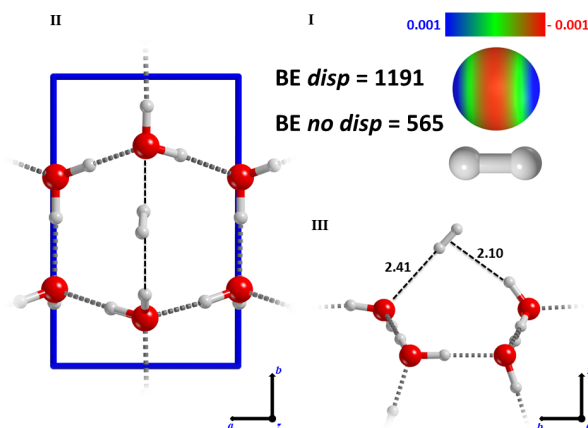


**Figure 16.** I) Representation of the hydrogen (H<sub>2</sub>) molecule along with its ESP surface, BSSE-corrected binding energies ( $BE$ ) with ( $disp$ ) and without ( $no\ disp$ ) dispersion. II) Top view of H<sub>2</sub>-(010) P-ice surface interaction (unit cell highlighted in blue). III) Detail of the side view.

## C. SURFACE DISTORTION ENERGY ON ASW

Hereafter we present the distortion energy contributions calculated on the amorphous slab will be compared with the same contributions calculated on the (010) P-ice model for some notable cases.

**Table 8.** Comparison of the distortion energy contributions (in Kelvin) calculated on the (010) P-ice slab and the mean value of these contributions calculated on the different adsorption cases on the amorphous ice model

Species	$\delta E_s$ crystalline ice	$\langle \delta E_s \rangle$ amorphous ice
CH <sub>3</sub> OH	662	2790
H <sub>2</sub> O	565	3211
HCN	589	1299
HCOOH	878	1660
NH <sub>3</sub>	734	1082

## D. BASIS SET A-VTZ\*

**Table 9.** Basis set for the H atom in CRYSTAL17 format used in this work

<b>H</b>	0		
S	3	1	
		34.06134	6.03E-03
		5.123575	4.50E-02
		1.164663	0.201897
S	1		
		0.32723	1
S	1		
		0.103072	1
P	1		
		0.8	1

**Table 10.** Basis set for the C atom in CRYSTAL17 format used in this work

C	0		
S	5	1	
		8506.038	5.34E-04
		1275.733	4.13E-03
		290.3119	2.12E-02
		82.0562	8.24E-02
		26.47964	0.240129
S	1		
		9.241459	1
S	1		
		3.364353	1
S	1		
		0.871742	1
S	1		
		0.363524	1
S	1		
		0.128731	1
P	4		
		34.7095	5.33E-03
		7.959088	3.59E-02
		2.378697	0.142003
		0.815401	0.342031
P	1		
		0.289538	1
P	1		
		0.100848	1
D	1		
		1.6	1
D	1		
		0.4	1

**Table 11.** Basis set for the N atom in CRYSTAL17 format used in this work

N	0		
S	5	1	
		11913.42	-5.23E-04
		1786.721	-4.04E-03
		406.5901	-2.08E-02
		114.9253	-8.12E-02
		37.10588	-0.23871
S	1		
		12.97168	1
S	1		
		4.730229	1
S	1		
		1.252518	1
S	1		
		0.512601	1
S	1		
		0.179397	1
P	4		
		49.21876	5.55E-03
		11.34894	3.81E-02
		3.428509	0.149414
		1.179951	0.348982
P	1		
		0.417261	1
P	1		
		0.142951	1
D	1		
		2	1
D	1		
		0.5	1

**Table 12.** Basis set for the O atom in CRYSTAL17 format used in this work

O	0		
S	5	1	
		15902.65	5.15E-04
		2384.954	3.98E-03
		542.7196	2.05E-02
		153.4041	8.03E-02
		49.54572	0.237668
S	1		
		17.33965	1
S	1		
		6.330336	1
S	1		
		1.699588	1
S	1		
		0.689545	1
S	1		
		0.23936	1
P	4		
		63.27052	6.07E-03
		14.62331	4.19E-02
		4.448952	0.161569
		1.528151	0.356828
P	1		
		0.529973	1
P	1		
		0.175094	1
D	1		
		2.4	1
D	1		
		0.6	1

**Table 13.** Basis set for the S atom in CRYSTAL17 format used in this work

S	0		
S	5	103954	2.47E-04
		15583.79	1.92E-03
		3546.129	9.96E-03
		1002.681	4.04E-02
		324.9029	0.130675
S	1	115.5123	1
S	2	44.52821	0.504036
		18.39789	0.230681
S	1	5.510068	1
S	1	2.125987	1
S	1	0.436919	1
S	1	0.157309	1
P	5	606.6937	2.32E-03
		143.507	1.86E-02
		45.74616	8.60E-02
		16.87291	0.252484
		6.63992	0.446327
P	1	2.672714	1
P	1	1.000009	1
P	1	0.354389	1
P	1	0.116713	1
D	1	1.1	1
D	1	0.275	1

**Table 14.** Basis set for the Cl atom in CRYSTAL17 format used in this work

Cl	0		
S	5	117805.8	2.42E-04
		17660.27	1.87E-03
		4018.597	9.74E-03
		1136.223	3.95E-02
		368.1206	0.127972
S	1	130.8615	1
S	2	50.47901	0.428741
		20.91681	0.196685
S	1	6.353139	1
S	1	2.494801	1
S	1	0.543359	1
S	1	0.194344	1
P	5	681.0688	2.37E-03
		161.1136	1.89E-02
		51.38664	8.78E-02
		18.95851	0.257074
		3.003516	0.371524
P	1	7.456529	1
P	1	1.060936	1
P	1	0.39452	1
P	1	0.133233	1
D	1	1.3	1
D	1	0.325	1